Quaternary Science Reviews 259 (2021) 106905

Contents lists available at ScienceDirect

Quaternary Science Reviews

journal homepage: www.elsevier.com/locate/quascirev

Climate and environmental changes of the Lateglacial transition and Holocene in northeastern Siberia: Evidence from diatom oxygen isotopes and assemblage composition at Lake Emanda

Svetlana S. Kostrova [a, b, *], Boris K. Biskaborn [a], Luidmila A. Pestryakova [c], Francisco Fernandoy [d], Marlene M. Lenz [e], Hanno Meyer [a]

[a] Alfred Wegener Institute Helmholtz Centre for Polar and Marine Research, Research Unit Potsdam, Telegrafenberg A45, Potsdam, 14473, Germany
[b] Vinogradov Institute of Geochemistry, Siberian Branch of Russian Academy of Sciences, Favorsky str. 1a, Irkutsk, 664033, Russia
[c] North-Eastern Federal University of Yakutsk, Institute of Natural Sciences, Belinskogo str. 58, Yakutsk, 677000, Russia
[d] Facultad de Ingeniería, Laboratorio de análisis isotópico, Universidad Andrés Bello, 980 Quillota St., Viña del Mar, 2531015, Chile
[e] Institute of Geology and Mineralogy, University of Cologne, Zülpicher Str. 49a, Cologne, 50674, Germany

ARTICLE INFO

Article history:
Received 18 December 2020
Received in revised form
10 March 2021
Accepted 10 March 2021
Available online 27 March 2021

Handling Editor: P Rioual

Keywords:
Stable isotopes
Diatoms
Climate changes
Lake sediments

ABSTRACT

A new dataset from Lake Emanda provides insights into climate and environmental dynamics in an extreme continental setting in northeastern Siberia. The $\delta^{18}O_{diatom}$ record is supported by diatom assemblage analysis, modern isotope hydrology and atmospheric circulation patterns. The data reveal a relatively cold oligotrophic freshwater lake system persisting for the last ~13.2 cal ka BP. Most recent $\delta^{18}O_{diatom}$ (+21.5‰) combined with present-day average $\delta^{18}O_{lake}$ (−16.5‰) allows calculating T_{lake} (~21 °C), reflecting summer conditions. Nonetheless, the $\delta^{18}O_{diatom}$ variability is associated with changes in $\delta^{18}O_{lake}$ rather than with T_{lake}. An obvious shift of ~2‰ in the $\delta^{18}O_{diatom}$ record at 11.7−11.5 cal ka BP accompanied by significant changes in diatom assemblages reflects the onset of the Holocene. Relatively high $\delta^{18}O_{diatom}$ during the Early Holocene suggests relatively warm and/or dry climate with associated evaporation effects. The absolute maximum in $\delta^{18}O_{diatom}$ of +27.7‰ consistent with high values of diatom indices at ~7.9−7.0 cal ka BP suggests a Mid Holocene Thermal Maximum. A continuous depletion in $\delta^{18}O_{diatom}$ since ~5.0 cal ka BP is interpreted as Middle to Late Holocene cooling reaching the absolute minimum at 0.4 cal ka BP (i.e. the Little Ice Age). An overall cooling trend (~0.3‰ 1000 yr^{-1}) throughout the Holocene follows decreasing solar insolation. The pattern of the Lake Emanda $\delta^{18}O_{diatom}$ record is similar to that obtained from Lake El'gygytgyn suggesting a common "eastern" regional signal in both records, despite their hydrological differences. Presently, atmospheric moisture reaches the study region from the west and east with ~40% each, as well as ~20% from the north.

1. Introduction

The high latitudes of the Northern Hemisphere (NH) are extremely sensitive to global climate changes due to various feedback processes (ACIA, 2005; Miller et al., 2010; IPCC, 2014). In particular, a continuous increase in Arctic air temperatures at twice the rate of the global average since 2014 (Overland et al., 2018) has led to a considerable reduction in Arctic sea ice cover (Snape and Forster, 2014; Letterly et al., 2018) and degradation of permafrost not only in the Arctic itself (Morgenstern et al., 2013; 2021; Aas et al., 2019; Biskaborn et al., 2019; Rudenko et al., 2020), but also in the adjacent territories (Streletskiy et al., 2015a; Opel and Ulrich, 2015; Ulrich et al., 2019; Biskaborn et al., 2019). Moreover, this strong global warming has induced a prolongation of the ice-free period in Arctic and sub-Arctic lakes and rivers (Shiklomanov and Lammers, 2014; Streletskiy et al., 2015b), an increase in evaporation (Wetterich et al., 2008; Fedorov et al., 2014) and lake water temperatures (Duff et al., 1999; Kumke et al., 2007) as well as major

* Corresponding author. Alfred Wegener Institute Helmholtz Centre for Polar and Marine Research, Research Unit Potsdam, Telegrafenberg A45, Potsdam, 14473, Germany.
E-mail addresses: Svetlana.Kostrova@awi.de (S.S. Kostrova), Boris.Biskaborn@awi.de (B.K. Biskaborn), lapest@mail.ru (L.A. Pestryakova), francisco.fernandoy@unab.cl (F. Fernandoy), mbaumer@uni-koeln.de (M.M. Lenz), Hanno.Meyer@awi.de (H. Meyer).

https://doi.org/10.1016/j.quascirev.2021.106905

changes in landforms such as formation of numerous thermokarst ponds and lakes (Smith et al., 2005; Jorgenson et al., 2006; Fedorov et al., 2014; Boike et al., 2016; Ulrich et al., 2019), land cover changes with expansion of tall shrubs and trees (Herzschuh et al., 2013; Frost and Epstein, 2014) and ecosystems (Pestryakova et al., 2012; Desyatkin et al., 2015; Khaliullina et al., 2016; Safronov, 2016). However, feedback mechanisms amplifying climatic changes in the northern high latitudes are still poorly understood and require a more detailed investigation of the natural variability at different time scales and in different climatic zones (Miller et al., 2010; Melles et al., 2019).

The central part of northeastern Siberia (60°–73°N, 120°–170°E; Fig. 1A) represents a distinctly continental region known for its climate extremes, with the Verkhoyansk Mountain Range being the coldest area in the NH (Shahgedanova et al., 2002). In contrast to other regions of northern Eurasia (Mangerud et al., 2004; Astakhov, 2018; Svendsen et al., 2019), this area was affected only by local glaciations during the last glacial period (Popp et al., 2007; Stauch and Lehmkuhl, 2010). Currently, despite the air temperature rise and associated permafrost degradation, over 80% of the territory is still underlain by continuous permafrost with thicknesses greater than 400 m (Desyatkin et al., 2015). In recent years, due to high sensitivity to global climate changes, northeastern Siberia has become a key region to study past climatic and environmental variability (Anderson et al., 2002; Müller et al., 2009; 2010; Werner et al., 2010; Nazarova et al., 2011; 2013; Biskaborn et al., 2012; 2016; Pestryakova et al., 2012; Herzschuh et al., 2013; Tarasov et al., 2013; Diekmann et al., 2016; Baumer et al., 2020; Vyse et al., 2020). The territory has a large number of lakes of various genesis and morphometry, storing in their sediments detailed information about climate, landscapes and hydrology since initial deposition (Zhirkov, 2000; Pestryakova et al., 2012). Their remote location implies that these lakes are sensitive archives for environmental/climatic reconstructions due to the reduced human impact in their catchments (Kumke et al., 2007; Pestryakova et al., 2012; Biskaborn et al., 2021).

To date, knowledge on lateglacial transition and Holocene climate and environment development in northeastern Siberia is rather limited and mainly based on pollen studies (Andreev et al., 1997; 2011; Anderson et al., 2002; Fradkina et al., 2005; Müller et al., 2009; 2010; Werner et al., 2010; Andreev and Tarasov, 2013; Herzschuh et al., 2013; Biskaborn et al., 2016), diatoms (Pestryakova et al., 2012; Biskaborn et al., 2012; 2016) and chironomid records (Nazarova et al., 2011; 2013). These studies have revealed a local to regional scale climate variability with noticeable differences in space and time (Biskaborn et al., 2012; 2016). In the central part of the region, an obvious shift occurred, from the colder and drier Younger Dryas to the Holocene with warmer and wetter conditions after 11.5 cal ka BP (calibrated calendar ages are used consistently in this study) accompanied by a substantial increase of shrub communities and a reduction of herbaceous taxa in vegetation cover (Müller et al., 2009; Werner et al., 2010). However, the Early Holocene was colder than today (Nazarova et al., 2013) and with prolonged seasonal lake-ice cover (Biskaborn et al., 2016). A notable climate warming, when air temperature reached its maximum during the Holocene, was reconstructed for the period between ~8.9 and 4.5 cal ka BP (Biskaborn et al., 2016) and accompanied by enhanced biological productivity (Nazarova et al., 2013) and spatial extent of forests (Anderson et al., 2002; Müller et al., 2009; 2010). After 4.8–4.5 cal ka BP, pronounced cooling is well recognized in the records (Müller et al., 2009; Nazarova et al., 2013; Biskaborn et al., 2016). Nevertheless, published qualitative reconstructions demonstrate a complex and partly controversial picture of climate and environment during the lateglacial transition and Holocene in northeastern Siberia (Anderson et al., 2002; Müller et al., 2009; Nazarova et al., 2013; Biskaborn et al., 2016). Therefore, isotope data from lakes in the region are helpful in resolving key questions related to palaeohydrology, as recently demonstrated by numerous diatom oxygen isotope records (Kostrova et al., 2013; 2014; 2019; Mackay et al., 2013; Meyer et al., 2015a; Narancic et al., 2016; Bailey et al., 2018; Swann et al., 2018; Cartier et al., 2019; Harding et al., 2020).

In this study, we aim to reconstruct the climatic and hydrological variability from a sediment core of Lake Emanda, located in the central part of northeastern Siberia (Fig. 1), a sparsely studied region, using diatom assemblage composition and diatom oxygen isotopes in the context of other relevant local and regional proxies. The combination of the state-of-the-art statistical evaluation of the diatom assemblage composition with the novel oxygen isotope composition of diatoms allows for a complementary assessment of the environmental conditions within a pristine, remote lake system.

The oxygen isotope composition of diatoms ($\delta^{18}O_{diatom}$), is used as an independent proxy commonly employed for palaeoenvironmental and/or climatic reconstructions (Swann and Leng, 2009; Sutton et al., 2018; van Hardenbroek et al., 2018). The $\delta^{18}O_{diatom}$ values are mainly driven by the temperature (T_{lake}) and the lake water isotope composition ($\delta^{18}O_{lake}$), in which diatom frustules grow. $\delta^{18}O_{lake}$ is in turn influenced by the isotope composition of precipitation ($\delta^{18}O_{prec}$) and other waters (inflow, outflow, and groundwater) as well as the degree of lake water evaporation (Leng and Barker, 2006). The $\delta^{18}O_{prec}$ signal depends on changes in air temperature (T_{air}) and is defined by the involved air mass trajectory (Dansgaard, 1964; Merlivat and Jouzel, 1979; Kurita, 2011). Variations in Lake Emanda $\delta^{18}O_{diatom}$ values are discussed according to these parameters, complemented by a diatom assemblage analysis of the same sedimentary sequence. Combined with other published regional environmental data (Anderson et al., 2002; Müller et al., 2009; 2010; Biskaborn et al., 2012; 2016; Nazarova et al., 2013; Tarasov et al., 2013; Ulrich et al., 2019) our new record is used to assess the environmental and climate dynamics in the region during the last ~13.2 cal ka BP.

2. Regional setting

Lake Emanda (65°17′N; 135°45′ E; 671 m a.s.l) is a large freshwater lake located in the permafrost zone, on the vast plateau of the eastern slope of the Verkhoyansk Mountain Range (Fig. 1). It extends for 8.3 km from north to south and has an average width of 3.5 km. The lake is heart-shaped and covers an area of 33.1 km^2. It has a maximum water depth of 15.8 m. The lake, occupying the Verkhoyansk-Kolyma orogenic region, is surrounded by ridges with elevations from 200 to 700 m (Oxman, 2003; Filatova and Khain, 2008). The bedrock comprises Palaeozoic to Mesozoic shelf sediments and turbidites deposited on the eastern margin of the north Asian craton (Oxman, 2003; Popp et al., 2007). The catchment area is ~179 km^2. The lake is a hydrologically open system fed by three small rivers with Synoptic River as the main inflow. The Seen (Syan) River outflows from the north part of the lake (Fig. 1B).

Lake Emanda is well mixed in the open water season with summer temperatures of up to 17–21 °C. The modern measured lake water pH varies between 6.7 and 7.0. The lake is typically ice-covered for more than half the year from early October to ice-out in late May (Glushkov, 2016). The lake is pristine and only subject to negligible anthropogenic impact and is therefore assumed to change primarily under the influence of natural factors.

The regional climate is continental with very cold, long winters and short but relatively warm summers. Average air temperatures range from −44.7 °C (January) to +13.0 °C (July) with an annual

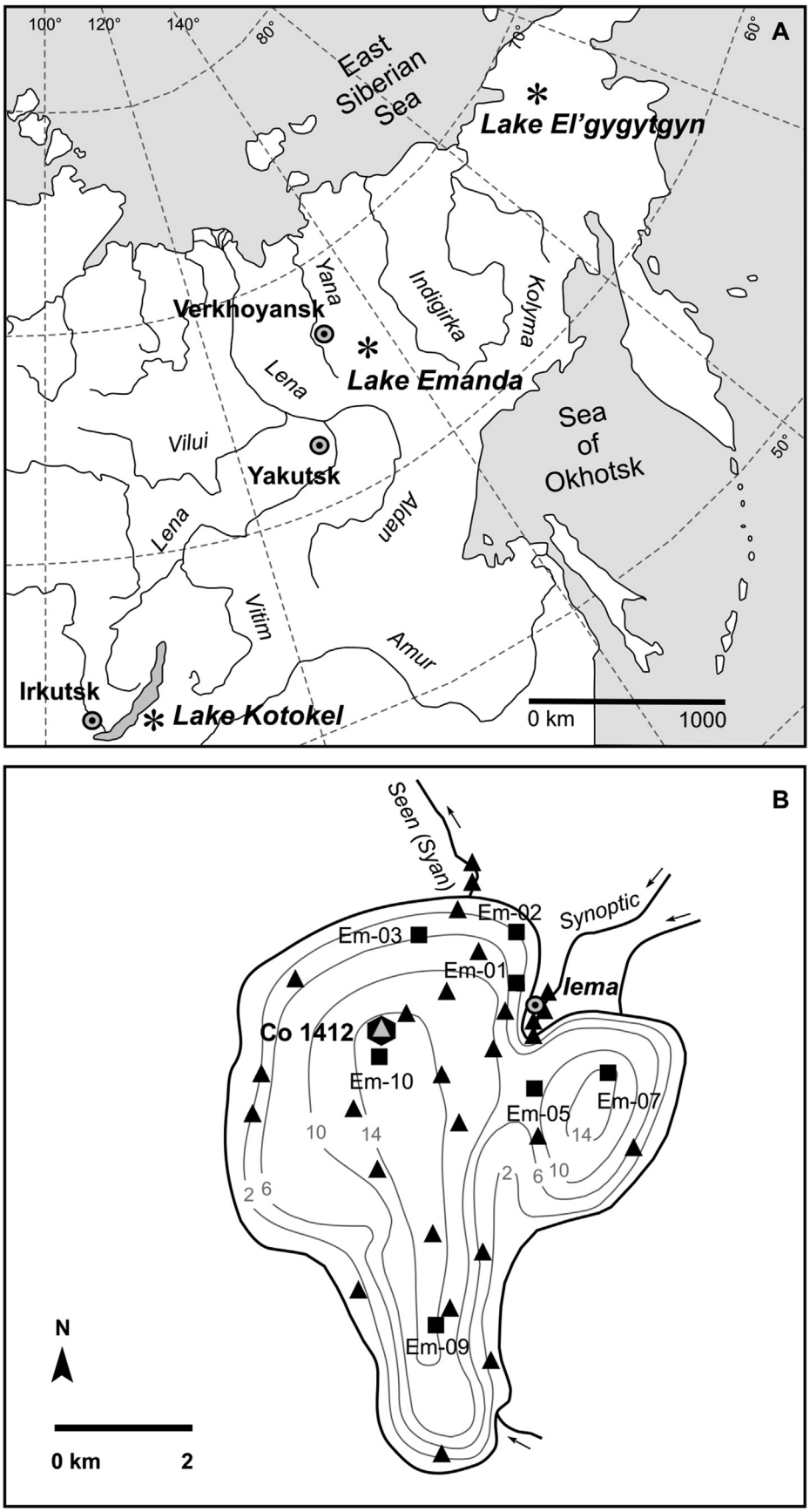

Fig. 1. Schematic maps showing (A) location of the study area in Eurasia; (B) Lake Emanda (65°17′N; 135°45′E; 671 m a.s.l) with location of the Iema meteorological station (65°17′N; 135°48′E; 671 m a.s.l), the Co1412 core (black hexagon), the surface sediment (black square), water depth profile (grey triangle) and water sampling sites (black triangle) used in this study. Bathymetry adapted from Baumer et al. (2020).

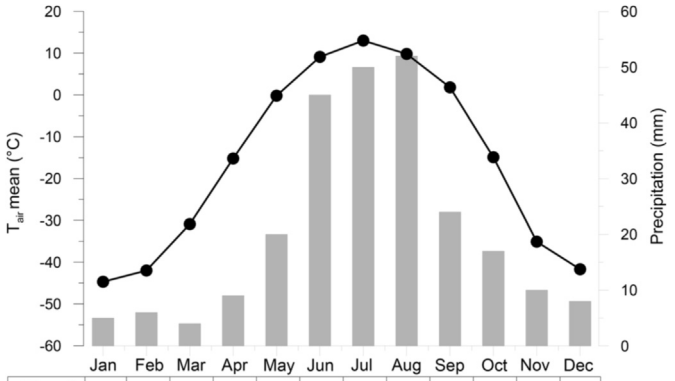

	Jan	Feb	Mar	Apr	May	Jun	Jul	Aug	Sep	Oct	Nov	Dec
$\delta^{18}O_{prec}$,‰	-36.0	-31.4	-27.8	-23.7	-18.0	-14.0	-13.8	-13.9	-15.8	-25.8	-30.8	-35.3
δD_{prec},‰	-286	-250	-217	-188	-141	-111	-109	-110	-126	-196	-239	-280

Fig. 2. Summary climate data for the Lake Emanda region: average monthly air temperature (black line) and average monthly precipitation amount (grey rectangle) based on meteorological data provided by the Hydrometcenter of Russia from 1961 to 1990 CE for the Iema station (available at: http://old.meteoinfo.ru/climatcities). The calculated mean monthly precipitation isotope data following Bowen (2020; The Online Isotopes in Precipitation Calculator, version OIPC3.1 from http://www.waterisotopes.org).

mean of −15.9 °C (1961–1990 CE; at the Iema station (65°17′N; 135°48′ E; 671 m a.s.l) located at the lake; Figs. 1B and 2). The annual precipitation is around 250 mm, with a maximum of 147 mm in the summer. The calculated mean annual $\delta^{18}O_{prec}$ and δD_{prec} isotope values at the Iema station are −26.6‰ and −208.4‰, respectively (Fig. 2; Bowen, 2020). The annual precipitation patterns are associated with the influence of cyclones and anticyclones in northeastern Siberia. The high-pressure cell (Siberian High) centered over northern Mongolia prevents moisture supply and increases radiation over the region leading to an extreme cooling during the winter. The advances of rare cyclones from the west/southwest are often accompanied by strong winds and prolonged snowstorms. Incursions of wet air masses from the Sea of Okhotsk may cause temporary temperature rise and snowfall (Wiese, 1927; Cherdonova (Atlasova), 1993). In summer, a low-pressure system dominates the region (Wiese, 1927). In contrast to the winter, increased influxes of moisture from the North Atlantic and the Arctic Ocean as well as easterly cyclones from the Sea of Okhotsk are notable (Cherdonova (Atlasova), 1993; Papina et al., 2017).

3. Materials and methods

3.1. Field campaign

In August 2017, a 6.1-m-long sediment core (Co1412; 65°18′ N, 135°46′ E; water depth: 14.6 m) was recovered using gravity and percussion piston corers (UWITEC Ltd., Austria) from the northwestern part of Lake Emanda (Fig. 1; Baumer et al., 2020). The core was split, described, and sub-sampled for sedimentological, biological and geochemical analyses at the University of Cologne, Germany. Additionally, surface sediment samples from different parts of the lake at varying depths (n = 8; Fig. 1B) were retrieved with a box-corer.

Water samples (Fig. 1B) were collected in August 2017 using a 1.5-L UWITEC water sampler equipped with a thermometer all over the lake from the surface (n = 23) and at the Co1412 coring site in a depth profile at semi-regular intervals (n = 10). Furthermore, water samples from the Synoptic River (inflow) at four different locations and from the Seen (Syan) River (outflow; n = 1) were taken. In total, 36 event-based precipitation samples were collected at the Iema station (Fig. 1B) from August to December 2017, covering every month at least five times. Water temperatures were also recorded. After sampling, all samples were stored cool in airtight bottles prior to isotope analyses.

3.2. Stable water isotope analysis

The stable oxygen ($\delta^{18}O$) and hydrogen (δD) isotope composition of water samples was measured using equilibration techniques with a Finnigan MAT Delta-S mass spectrometer at AWI Potsdam, Germany. The analytical uncertainty (1σ) is ±0.1‰ and ±0.8‰ for $\delta^{18}O$ and δD, respectively (Meyer et al., 2000). The secondary parameter deuterium excess is calculated as $d = \delta D - 8 \cdot \delta^{18}O$ (Dansgaard, 1964). Data are given as per mil difference (‰) to V-SMOW.

3.3. Identification of modern air masses and moisture provenance

Five-day air-parcel backward trajectories were calculated both for a total of 365 days and for the 36 days of 2017 with collected precipitation events at the Iema meteorological station (Fig. 1B) to identify the air masses and moisture provenance using the freely available hybrid single-particle Lagrangian integrated trajectory (HYSPLIT) model (Draxler and Hess, 1998; Draxler and Rolph, 2015; Stein et al., 2015). Most of tropospheric moisture is contained up to 2,000 m agl (above ground level). To avoid any low-altitude topographical interferences (Krklec and Domínguez-Villar, 2014), calculations were made running single backward trajectories arriving at 1,500 m agl (around pressure level of 850 hPa) for 120 h back from the starting date (at 12:00 h local time). Single trajectories were combined into three main clusters, following a statistical treatment until minimal differences between trajectories within a cluster and maximal differences between clusters were reached and a further decrease in the number of clusters led to a significant increase in the total spatial variance (Draxler and Rolph, 2015).

3.4. Core lithology and chronology

In this study, the upper 123 cm-long section of the Co1412 core from the Lake Emanda sediments was chosen for diatom oxygen isotope investigation due to the presence of diatoms only to this depth. The study of Baumer et al. (2020) has revealed that the selected part is composed of fine-grained hemipelagic diffusely-layered sediments varying in their color from beige to brown (Fig. 3) and has been deposited during the last ~13,220 years. The Co1412 core chronology for the studied section is based on the modern sediment surface (2017 CE) and two ^{14}C dates on terrestrial plant fragments at 51.5 cm (4695 ± 167 ^{14}C yr; 5290 ± 233 cal yr BP) and at 98.5 cm (9269 ± 285 ^{14}C yr; 10190 ± 238 cal yr BP). The Bayesian age-depth model (Fig. 3) was calculated in R version 3.4.1 (R Core Team, 2017) with the Bacon software package version 2.3.6 (Blaauw and Christen, 2011). The software calibrates radiocarbon dates to calendar years before present (1950 CE) using the IntCal13 calibration curves (Reimer et al., 2013). The complete age-depth model for the sediment core is presented and discussed in detail in Baumer et al. (2020).

3.5. Analysis of diatom assemblage composition

In total, 92 sediment samples from the whole Co1412 core, were processed for diatom analysis using a consistent treatment with H_2O_2 (30%) and HCl (10%) for removing organic and calcareous components (Pestryakova et al., 2012; 2018). Diatom samples were mounted on microscope slides with Naphrax® and analysed with a Zeiss-Axioplan-microscope equipped by differential interference contrast (Nomarski) optics at a magnification of 1000 ×. About 500

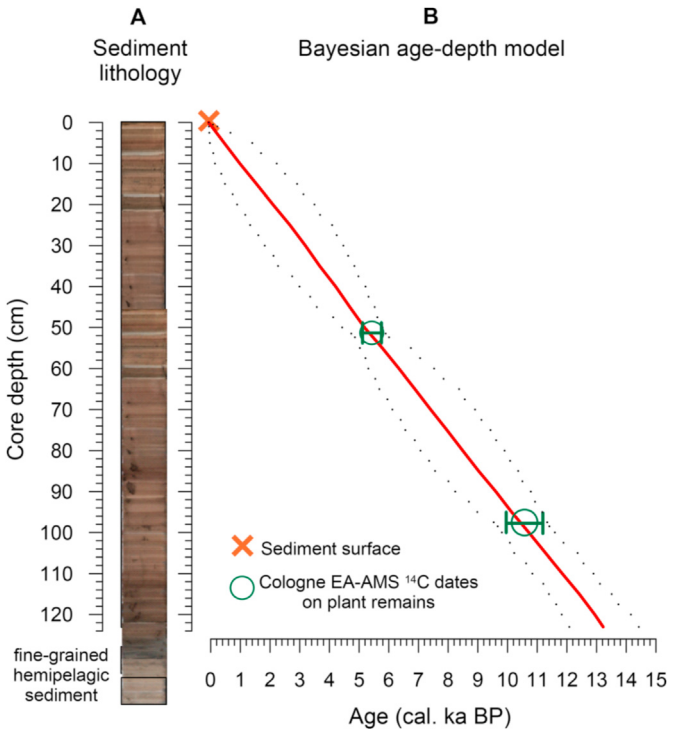

Fig. 3. (A) Sediment lithology (Baumer et al., 2020) and (B) Bayesian age-depth model for the upper 123-cm section of the Co1412 core, based on the modern sediment surface (2017 CE) and two ^{14}C AMS dates on plant remains, adopted from Baumer et al. (2020). (For interpretation of the references to color in this figure legend, the reader is referred to the Web version of this article.)

diatom valves per slide were counted along random transects. However, only 105 valves could be counted in the samples at 105–123 cm depth because diatom concentrations were low. No or only single diatoms occurred further down core. Diatom concentrations ($\times 10^6$ valves g^{-1} of dry sediment) were calculated according to the method outlined by Davydova (1985). Species abundance data were converted from counts to percentages. Taxonomic identification followed Gleser et al. (1974; 1988; 1992); Komarenko and Vasilyeva (1975); Krammer (2000; 2002; 2003); Krammer and Lange-Bertalot (1991; 1999a; 1999b; 2000); Lange-Bertalot (2001); Loseva (2000), and Makarova et al. (2002). The classification of diatom taxa with regard to their preferred habitat followed the system proposed by Round et al. (1990) and information given in Krammer and Lange-Bertalot (1991; 1999a; 1999b; 2000). Hereby we distinguished between planktonic (floating in water), epiphytic (attached to algae), and epipelic/epipsammic (on mud or sandy ground). For simplification, we further use the term "benthic" as equivalent to non-planktonic taxa (including epiphytic and epipelic/epipsammic).

For statistical analysis of the species abundance data, the R environment for multivariate statistical analysis (R Core Team, 2012) was used. Diatom zone boundaries were defined using a constrained incremental sums-of-squares clustering (CONISS) on all species counts after chi squared standardization and with using Bray Curtis dissimilarity index (Grimm, 1987). A detrended correspondence analysis (DCA) was performed to calculate gradient length in standard deviation (SD) units for the diatom data set using the 'decorana' function in the package 'vegan' (Oksanen et al., 2020). Because the gradient length (SD = 2.1) was below 2.5 (Birks, 2010), principal component analysis (PCA) axes scores were chosen as a suitable ordination method to reveal major downcore trends in diatom assemblage data. PCA was performed on filtered and square-root transformed data using the 'prcomp' function in the basic R package 'stats'. The filter was set to ≥2.5% in ≥2 samples. PCA was based on Euclidean distance; k-means clustering with 95% confidence ellipses was calculated using the 'kmeans' function (centers 4) in the 'stats' package. Diatom species richness and Hill's N2 diversity (Hill, 1973) were calculated using raw diatom counts rarefied to the minimum base sum (n = 280). Rarefaction corrects diversity estimates for sampling differences (Birks et al., 2016). Hill's diversity number N0 was used to calculate species richness as the realistic total number of taxa in a sample after rarefaction. N1 (exponential of Shannon index) was used to amplify "typical species", and N2 (inverse of the Simpson concentration) in which each taxon is weighted by its squared relative abundance to amplify abundant species and discounts rare species (Chao et al., 2014). Rarefaction, richness, and diversity indices were calculated using the 'vegan' package in R (Oksanen et al., 2020).

3.6. Diatom oxygen isotope analysis

Nine surface sediment samples (Table 1) and a total of 46 sediment samples (Fig. 4A) from the upper part (0–123 cm) of the core which contained diatoms were processed for $\delta^{18}O_{diatom}$ analysis with an average temporal resolution of 284 years throughout the past ~13.2 ka. Separation and cleaning of diatoms from the sediment matrix was carried out using a multistep process of chemical digestion, sieving, and heavy liquid separation (HLS) described in detail in Kostrova et al. (2019). This procedure includes H_2O_2 (35%) and HCl (10%) treatment to remove organic matter and eliminate carbonates, respectively, as well as a centrifuging in a sodium polytungstate (SPT; $3Na_2WO_49WO_3{\cdot}H_2O$) solution (2.50–2.14 g cm^{-3}) to separate diatoms from the terrigenous fraction. This fraction was retained for a contamination assessment and $\delta^{18}O_{diatom}$ correction. An inverse HLS consisting of drop-by-drop water addition to the initial SPT solution of 2.18 g cm^{-3} was applied to extract hardly soluble micro-organics and lighter contaminants. The water addition was continued until all heavier particles including the diatoms settled to the bottom of the plastic tube, whilst the hardly soluble micro-organic and lighter contaminants were collected from the SPT solution surface. After the final HLS step, samples were washed in ultra-pure water using a cellulose nitrate membrane with a 3 μm pore size to remove potential clay minerals and/or broken diatom fragments.

All purified diatom samples were assessed for contamination using Energy-Dispersive X-ray Spectroscopy (EDS) under a ZEISS ULTRA 55 Plus Schottky-type field emission scanning electron microscope (SEM) equipped with a silicon drift detector (UltraDry SDD) (3 repetitions, an acceleration voltage of 20 kV; excited area size of 100–200 μm, measuring time of 0.5 min; Chapligin et al., 2012a; Kostrova et al., 2019). According to the EDS data (Table 1; Fig. 4B), all prepared diatom samples were exceptionally pure, comprising between 98.2 and 99.8% SiO_2, and 0.1–0.9% Al_2O_3 and, hence, were suitable for $\delta^{18}O_{diatom}$ analysis.

The laser fluorination method (Chapligin et al., 2010) was applied to measure $\delta^{18}O_{diatom}$ (n = 30) and $\delta^{18}O_{cont}$ (terrigenous contaminant fraction; n = 3) at AWI Potsdam, Germany. The outer hydrous layer of the diatom valves was removed using an inert gas flow dehydration (iGFD) at 1100 °C under argon gas (Chapligin et al., 2010). This was followed by a full reaction with a BrF_5 reagent to liberate oxygen (Clayton and Mayeda, 1963), which was then separated from byproducts and directly measured against an oxygen reference sample of known isotopic composition with a PDZ Europa 2020 mass spectrometer. Replicate analyses of the calibrated working standard BFC (Chapligin et al., 2011) yielded $\delta^{18}O$ = +28.80 ± 0.30‰ (n = 34) indicating an accuracy and analytical reproducibility similar to the methods long-term

Table 1
Surface sediment samples from Lake Emanda used in the study. Main geochemical characteristics of diatoms based on EDS data. Measured $\delta^{18}O$ values ($\delta^{18}O_{meas}$) and $\delta^{18}O$ values corrected for contamination ($\delta^{18}O_{corr}$) are given.

Sample name	Latitude	Longitude	Water depth (m)	Characteristics of purified diatom samples			
				SiO_2 (%)	Al_2O_3 (%)	$\delta^{18}O_{meas}$ (‰)	$\delta^{18}O_{corr}$ (‰)
Em-01	65°17	135°48	2.2	98.3	0.2	+20.9	+21.0
Em-02	65°18	135°47	3.2	99.0	0.2	+21.5	+21.6
Em-03	65°18	135°46	5.9	99.3	0.2	+21.2	+21.3
Em-05	65°16	135°48	8.3	98.3	0.4	+21.4	+21.6
Em-07	65°17	135°49	15.4	98.4	0.2	+21.5	+21.7
Em-09	65°15	135°46	13.5	98.3	0.4	+20.6	+20.7
Em-10	65°17	135°45	15.8	98.7	0.1	+22.3	+22.4

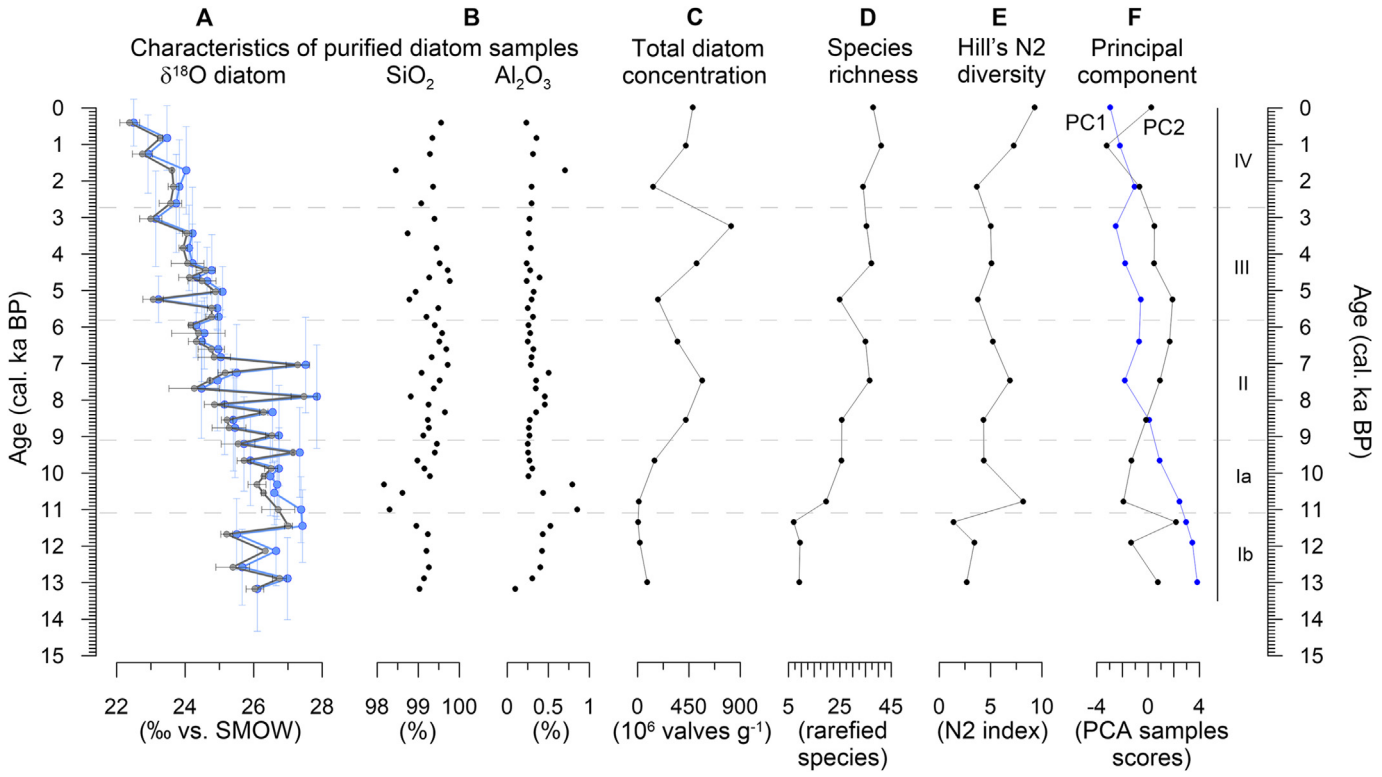

Fig. 4. Summary data for diatom samples from the Lake Emanda Co1412 core: (A) measured $\delta^{18}O_{meas}$ (grey line) shown with analytical errors and contamination-corrected $\delta^{18}O_{corr}$ values of diatoms (blue line) shown with chronological errors and (B) SiO_2 and Al_2O_3 concentrations in the purified diatom samples analysed by EDS and measured for $\delta^{18}O$; (C) total diatom concentration, (D) species richness and (E) Hill's N2 diversity are plotted next to (F) the first two principal components (PC) sample scores (PC1 – blue line; PC 2 – black line). (For interpretation of the references to color in this figure legend, the reader is referred to the Web version of this article.)

analytical reproducibility (1σ) of ±0.25‰ (Chapligin et al., 2010).

The measured $\delta^{18}O$ signal ($\delta^{18}O_{meas}$) was contamination corrected ($\delta^{18}O_{corr}$) using a geochemical mass-balance approach (Swann and Leng, 2009; Chapligin et al., 2012a):

$$\delta^{18}O_{corr} = \left(\delta^{18}O_{meas} - \delta^{18}O_{cont} \cdots c_{cont}/100\right)/(c_{diatom}/100) \quad (1)$$

where $\delta^{18}O_{cont} = +13.8 \pm 0.1$‰ (n = 3) represents the average $\delta^{18}O$ of the terrigenous fraction after the first heavy liquid separation. The percentages of contamination (c_{cont}) and diatom material (c_{diatom}) within the analysed sample have been calculated using the EDS-measured Al_2O_3 content of the individual sample divided by the average Al_2O_3 content of the contamination (17.4 ± 0.19% in terrigenous fractions, n = 3) and as (100%–c_{cont}), respectively.

4. Results

4.1. Water isotopes

Water isotope data for Lake Emanda, rivers connected to the lake and regional precipitation are presented in a $\delta^{18}O$–δD diagram (Fig. 5) and summarized in Table 2.

The modern $\delta^{18}O_{lake}$ and δD_{lake} values are relatively constant and vary between −16.7‰ and −16.4‰ (mean: −16.5‰) and from −139.0‰ to −137.1‰ (mean: −137.8‰), respectively. The *d* excess changes from −6.0‰ to −4.9‰ with a mean value of −5.6‰. The outflow (Seen River) displays mean $\delta^{18}O = -16.4$‰ and $\delta D = -137.5$‰ (*d* excess: −5.9‰) comparable to the mean lake values. Synoptic River draining into Lake Emanda shows a lower mean $\delta^{18}O$ value of −18.6‰ and δD of −144.6‰ (mean *d* excess = +4.1‰). The stable isotope composition of local precipitation sampled at the Iema station between August and

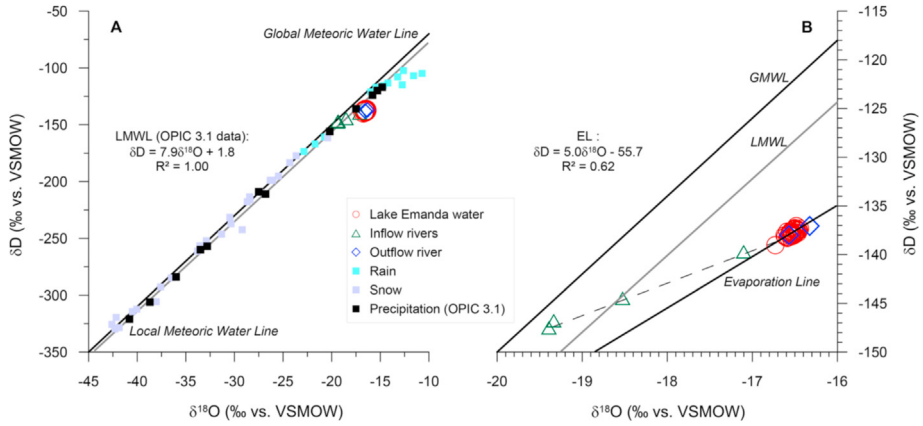

Fig. 5. $\delta^{18}O$–δD diagram for water samples. (A) Lake Emanda and rivers connected to the lake as well as precipitation. (B) Lake Emanda hydrology. Additionally, the Global Meteoric Water Line (GMWL; $\delta D = 8 \cdot \delta^{18}O + 10$; Craig, 1961; Rozanski et al., 1993) and Local Meteoric Water Line (LMWL) based on OPIC 3.1 calculated data (Bowen, 2020) as well as an evaporation line (EL) for Lake Emanda waters are given. Dotted line demonstrates a mixing of the lake and Synoptic River waters.

December varies in wide range from −42.6 to −10.7‰ for $\delta^{18}O_{prec}$, and from −329.8 to −102.3‰ for δD_{prec} (the *d* excess is from −19.3 to +17.8‰). Precipitation has not been collected from January through July.

4.2. Modern air masses and moisture provenance

HYSPLIT analyses carried out to identify the pathways of air masses reaching the study area, exhibit a wide distribution of the trajectories during the year 2017 (Fig. 6A). Statistical evaluation (Draxler and Rolph, 2015) revealed the three most common directions of air masses supplying moisture to the region. Among the identified air masses arriving at Iema station, about 41% originated from the west/northwest, over the Gydan Peninsula and the Kara Sea coast (cluster 1) and about 40% approached the region from the south/southeast originating at the border of the Sea of Okhotsk around the Suntar-Khayata Range (cluster 2). About 19% of air masses arrived from the northeast, from the East Siberian Sea (cluster 3).

A similar pattern was recognized for the 36 precipitation events registered between August and December 2017. However, moisture pathways approaching the region slightly differed in origin and contribution of each calculated cluster (Fig. 6B). In the second part of the year 2017, about 39% of precipitation events derived from the west (cluster 1) and originating at around 60° N and 90° E. These air masses are characterized by the highest mean isotope values of $\delta^{18}O_{prec} = -23.7‰$, $\delta D_{prec} = -185.9‰$ (*d* excess = +3.9‰). About 36% of collected precipitation (cluster 2) with mean $\delta^{18}O_{prec}$ and δD_{prec} values of −27.4‰ and −213.4‰, respectively (*d* excess = +6.0‰) originated from the Sea of Okhotsk at around 55°N and 136°E following a path over the sea and then heading north. Cluster 3 included 25% of air parcels originating from the north/northeast, over the Eastern Siberian Sea and represented the most depleted precipitation with an average $\delta^{18}O_{prec}$ of −33.4‰, δD_{prec} of −259.3‰ (*d* excess = +7.6‰).

4.3. Diatom record

Within the Co1412 core sediments, the upper interval (0–123 cm; upper ~13.2 cal ka BP) represented by 15 samples contained diatoms, whereas no or single diatoms occurred in the lower interval (123–606 cm; ~13.2–56.5 cal ka BP), eliminating it from further analysis. Diatom frustules are well preserved and show no sign of dissolution. The flora is diverse and the fossil diatom assemblages comprise 101 diatom taxa from 48 genera in total. Of these, 23 taxa account for >75% of all diatoms present in every samples. These include taxa mainly belonging to the genera *Pinnularia*, *Aulacoseira*, *Stauroneis*, and *Navicula*. Species with a relative abundance ≥2% in at least one stratigraphic level are presented in Fig. 7. Guided by the CONISS cluster analysis, the percentage diagram is divided into four diatom zones (DZ) of which zone I is subdivided into zone Ia and Ib, because Ib only consists of two samples and hence was not attributed a full zone.

DZ-I consisting of subzones Ia and Ib (123–85.5 cm; ~13.2–9.1 cal ka BP) is dominated by benthic *Staurosirella pinnata* (4.4–51.2%) and *Staurosira venter* (1.4–30.2%) (Haworth, 1975), of which both species are most abundant with maximum peaks in subzone Ia (Fig. 7). The planktonic species *Cyclotella iris* (5.4–84.3%) reaches its prominent high at 105.5 cm (11.3 cal ka BP) leading to a peak in planktonic forms which are generally low in DZ-I. A few

Table 2
Summary of stable isotope data ($\delta^{18}O$, δD and *d* excess), including minimum, mean and maximum values, standard deviations (SD) as well as slopes and intercepts from the $\delta^{18}O$–δD diagram for the analysed samples of Lake Emanda water, water from rivers connected to Lake Emanda (collected in August 2017) and precipitation water (collected in August–December 2017).

Sample type	No. total	$\delta^{18}O$ (‰) min	$\delta^{18}O$ (‰) mean	$\delta^{18}O$ (‰) max	$\delta^{18}O$ (‰) SD	δD (‰) min	δD (‰) mean	δD (‰) max	δD (‰) SD	*d* (‰) min	*d* (‰) mean	*d* (‰) max	*d* (‰) SD	Slope	Intercept	R^2
Lake Emanda	33	−16.7	−16.5	−16.4	0.1	−139.0	−137.8	−137.1	0.4	−6.0	−5.6	−4.9	0.3	5.0	−55.7	0.62
Inflow (Synoptic River)	4	−19.4	−18.6	−17.1	1.1	−147.5	−144.6	−139.7	3.5	−2.9	+4.1	+7.9	5.0	3.3	−83.4	0.99
Outflow (Seen (Syan) River)	2	−16.6	−16.4	−16.3	0.2	−138.0	−137.5	−137.1	0.7	−6.5	−5.9	−5.4	0.7	3.9	−74.0	1.00
Rain	13	−22.9	−15.9	−10.7	4.1	−173.5	−128.2	−102.3	26.7	−19.3	−0.9	+9.3	9.1	6.3	−27.7	0.95
Snow	26	−42.6	−33.1	−23.7	6.2	−329.8	−256.0	−177.3	50.3	−8.8	+8.8	+17.8	5.3	8.0	+9.3	0.99

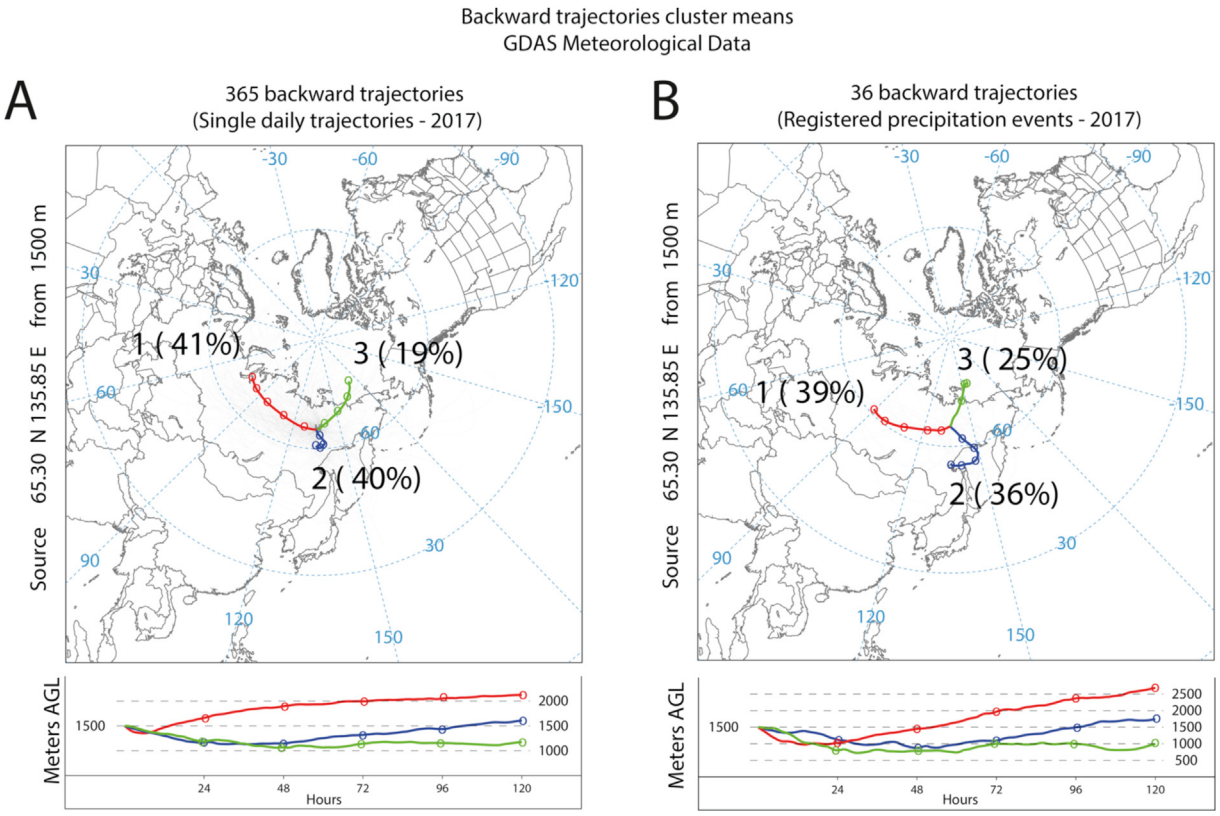

Fig. 6. Backward trajectories analysis (5 days, 120 h) for (A) a total of 365 single trajectories calculated at pressure level of 850 hPa for the whole year 2017 and (B) all registered and sampled single precipitation (n = 36) events between August and December 2017. Thin light-grey lines represent each single trajectory used to compute the cluster analysis in bold color lines. Three main trajectory directions (or clusters) were identified in both scenarios (1–3 each with the percentage of the total representation): green shows a north component and lower elevation path, red lines are long distance and high elevation transport paths from the east and blue lines are shorter transport from the south and medium altitudes (see lower panel). (For interpretation of the references to color in this figure legend, the reader is referred to the Web version of this article.)

benthic species, *Ellerbeckia arenaria*, *Amphora ovalis*, *Cavinula jaernefeltii*, and *Navicula* spp., and planktonic *Lindavia (Cyclotella) bodanica* do not exceed 1–3% in their abundance. A large increase in the species richness (from 7 to 20 species; Fig. 4D) and Nill's N2 diversity (from 1.4 to 8.2; Fig. 4E) is accompanied by increasing abundances of benthic taxa making up ~75% of the total diatom assemblage in the sample at 100.5 cm (10.8 cal ka BP). Total diatom concentration (TDC; Fig. 4C) is relatively low with the absolute minimum of 4×10^6 valves g^{-1} at 105.5 cm (11.3 cal ka BP). The interval between 105 and 90 cm (11.2 and 9.6 cal ka BP) is dominated by epipelic/epipsammic *S. pinnata* (17.8%) and *S. venter* (9.2%), *Cavinula cocconeiformis* (14.8%) and *Navicula* spp. (11.3%), and planktonic *L. bodanica* (19.4%). Decreases in abundances of benthic taxa occur after 90 cm (9.6 cal ka BP), concurrent with increases in abundances of planktonic species *C. iris* (up to 27.5%) and *L. bodanica* (up to 37.7%; Fig. 7).

DZ-II (85.5–55.5 cm; 9.1–5.8 cal ka BP) is mainly characterised by co-dominant occurrence of the planktonic species *C. iris* (16.8–40.1%) and *Aulacoseira ambigua* (22.1–31.5%; Fig. 7). In DZ-II, the TDC (maximum 565×10^6 valves g^{-1} at 70 cm; 7.4 cal ka BP; Fig. 4C), species richness (25–37; Fig. 4D) considerably increased as compared to DZ-I. Nill's N2 diversity (4.3–6.8) is slightly higher on average than in DZ-I (Fig. 4E). Diversity changes are related to increasing abundances of several benthic taxa (Fig. 7), such as naviculoid species *Pinnularia nodosa* (7.9%) and *Sellaphora pupula* (2.5%).

DZ-III (55.5–25.5 cm; 5.8–2.7 cal ka BP) is further dominated by *C. iris* (41.4–47.1%) while *Pantocsekiella tripartita* (6.2–16.4%) occur as another dominant taxon (Fig. 7). Zone III differs from zone II by a total disappearance of *A. ambigua*. Generally, the abundance of planktonic species gradually decreases, paralleled by increasing abundance of benthic taxa. *P. nodosa* (5.2–12.1%) and *S. pupula* (2.2–7.7%) dominate the benthic assemblages. TDC in DZ-III (Fig. 4C) is the highest in the entire core record at 30 cm (3.2 cal ka BP) with 819×10^6 valves g^{-1}, and the diversity indices stay comparable to DZ-II (Fig. 4).

DZ-IV (25.5–0 cm; 2.7–0 cal ka BP) demonstrates continuing dominance of *C. iris* (23.6–51.2%). *Pantocsekiella (Cyclotella) ocellata* appears in notable abundances (up to 9.9%) in the interval 20.5–10.5 cm (2.2–1.0 cal ka BP), while *P. tripartita* reaches its maximum of 18.1% in the surface sample (Fig. 7). A slight increase in benthic species with minor abundances leads to maximum values in Hill's N2 diversity in the surface sample (Fig. 4E).

The PCA reveals that the main patterns of stratigraphic changes in the diatom assemblage, shown in the first two principal component axes (Figs. 4F and 8), represent 52% of the total species variance. PC1 mainly represents variance corresponding to the change from small benthic fragilarioid species and *L. bodanica* towards other planktonic and benthic species appearing around 80 cm in the core (Fig. 8). PC2 characterises variance between diatom zones II + III in the positive vector and diatom zone IV in the negative vector (Fig. 8).

4.4. Oxygen isotope record

The Co1412 core diatom $\delta^{18}O_{corr}$ values (further referred to as $\delta^{18}O_{diatom}$) range from +22.5‰ to +27.8‰ (mean: +25.3‰) and follow the same trend as $\delta^{18}O_{meas}$ values, but are, on average, about

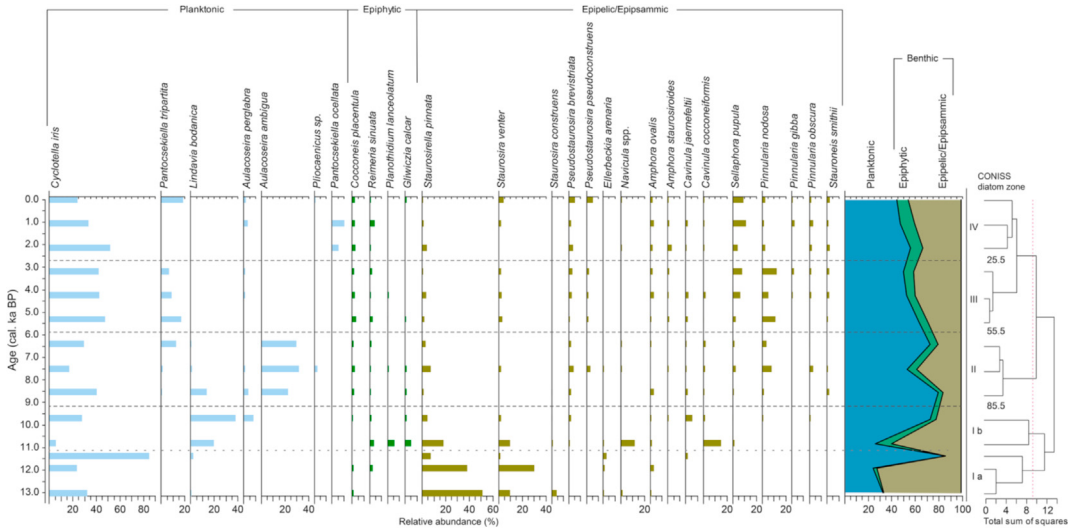

Fig. 7. Relative abundances of the most common diatom species in the sediment core Co1412 from Lake Emanda, grouped by habitat preference. Diatom zonation was guided by the CONISS cluster analysis.

0.2‰ higher (Fig. 4A), which is within the analytical error. Hence, the contamination correction is low and has no significant influence on the pattern of the downcore record.

The interval from 13.2 to 11.7 cal ka BP displays relatively low $\delta^{18}O_{diatom}$ values with noticeable variations between +25.5 and + 26.7‰ gradually decreasing with time. After a sharp rise to +27.4‰ at 11.5 cal ka BP, $\delta^{18}O_{diatom}$ values show a stepwise decrease to +25.9‰ from 11.0 to 9.7 cal ka BP). Frequent variations of ~1–3‰ are revealed in the interval of 9.7–6.8 cal ka BP when the $\delta^{18}O_{diatom}$ values reach the absolute maximum of +27.8‰ at 7.9 cal ka BP. After a sharp decline to +24.5‰ at 7.7 cal ka BP, and subsequent rise to +27.5‰ at 7.0 cal ka BP, the $\delta^{18}O_{diatom}$ abruptly drops to +25.0‰ by 6.8 cal ka BP and then slightly varies around +24.8‰ between 6.8 and 5.5 cal ka BP. A pronounced minimum of +23.2‰ is registered at 5.2 cal ka BP. After 5.0 cal ka BP, $\delta^{18}O_{diatom}$ values gradually decline reaching the absolute minimum of +22.5‰ at 0.4 cal ka BP. In general, a gradual depletion of ~4‰ in $\delta^{18}O_{diatom}$ is observed throughout the record.

Surface diatom samples from Lake Emanda demonstrate a spatially rather homogeneous isotope signal varying from +20.7 to +22.4‰ (Table 1). Small differences could be due to slightly different age of the samples, as a box-corer does not allow for undisturbed sampling of surface samples.

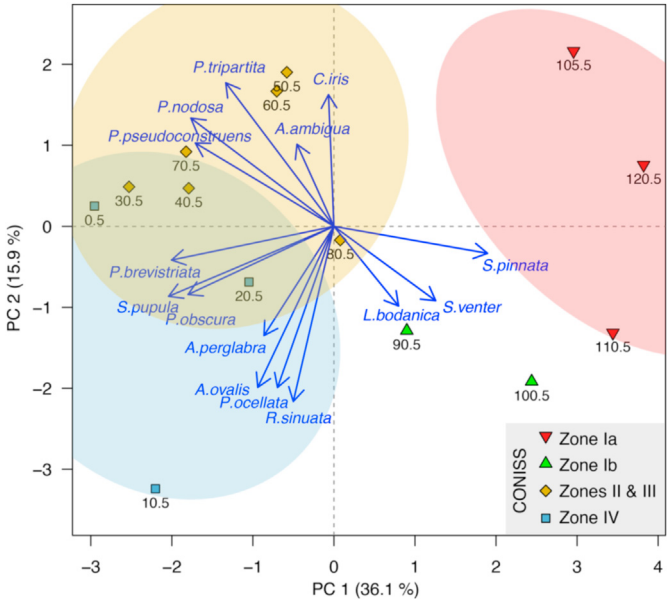

Fig. 8. Biplot of the first two principal components (PC 1 and 2) calculated using a principal component analysis (PCA) on diatom species data. Species shown are filtered according to their occurrence at ≥ 2.5% in ≥2 samples. Ellipses represent 95% confidences of k-means clusters generated form the filtered data, matching boundaries suggested by the CONISS analyses (Fig. 7).

5. Discussion

5.1. Isotope hydrology and meteorological background

An understanding of the modern hydrological and meteorological patterns is particularly important for decoding information about past climate and environmental conditions stored in diatom oxygen isotope records (Kostrova et al., 2013; 2014; 2019; 2020; Mackay et al., 2013; Meyer et al., 2015a; Bailey et al., 2018; Swann et al., 2018; Harding et al., 2020).

Stable isotope data for precipitation collected at the Iema station from August to December indicate distinct (about 20‰) seasonal differences (Table 2) comparable to those calculated by Bowen (2020; Fig. 2). Collected rain samples characterise the late-summer conditions with the higher mean $\delta^{18}O_{prec}$ and δD_{prec} values of −16‰ and −128‰, respectively (mean *d* excess = −0.9‰). Snow samples recorded from mid-September display the colder season with lower mean $\delta^{18}O_{prec}$ = −33‰ and δD_{prec} = −256‰ (mean *d* excess = +8.8‰). This indicates a clear seasonality both in δ-values and *d* excess for the precipitation arriving at Lake Emanda and the Iema station. The warm season precipitation is strongly influenced by secondary fractionation processes (such as admixture of water vapour from open water bodies, indicated by low *d* excess), not visible in the cold season precipitation.

In summer, snow melt water from the hinterland may supply Lake Emanda via inflow rivers. This is supported by the relatively lighter isotope composition of Synoptic River ($\delta^{18}O_{SR}$: between −19.4 and −17.1‰; Table 2) compared to $\delta^{18}O_{lake}$ (Table 2). These $\delta^{18}O_{SR}$ values show a gradual increase of ~2‰ with decreasing distance to the river mouth (Fig. 1B). This could indicate

a progressive mixing of the lake and river waters downstream (Fig. 5B). The *d* excess of Synoptic River of +4.1‰ is substantially higher than that of the lake (−5.6‰; Table 2), pointing to no significant evaporation processes in the catchment.

In contrast, the isotopic composition of the Lake Emanda water does not show significant changes and varies in a narrow range around average values of −16.5 ± 0.1‰ (n = 33) for $\delta^{18}O_{lake}$, −137.8 ± 0.4‰ for δD_{lake} and a mean *d* excess of −5.6 ± 0.3‰ (Table 2). A water isotope profile from the surface to 14.3 m depth also exhibits a narrow range of ±0.07‰ for $\delta^{18}O$ (Fig. 9A). These values indicate a well-mixed lake water environment in mid-summer, which is supported by a lack of significant temperature differences between surface and bottom water (Fig. 9B). There is no correlation between $\delta^{18}O_{lake}$ and T_{lake} (R^2 = 0.16; n = 31). The δ-values of lake samples plot below the GMWL (Fig. 5) and linearly correlate with a slope of 5.0 and an intercept of −55.7 (R^2 = 0.62), indicating substantial evaporative enrichment of the lake water, even when comparing the isotope composition of Lake Emanda water to measured summer precipitation at the Iema station (which has a similar $\delta^{18}O$, but a higher *d* excess of −0.9‰). Local evaporation effects of lake waters are distinctly expressed for numerous Yakutian lakes (Wetterich et al., 2008). The intersection point of the evaporation line (EL; Fig. 5) and GMWL is at about −23.0‰ for $\delta^{18}O_{lake}$ and at −170‰ for δD_{lake} and, hence, quite similar to annual average values of $\delta^{18}O_{prec}$ = −21.7‰ and δD_{prec} = −171‰ (Bowen and Revenaugh, 2003; Bowen, 2020), but lower than the mean isotopic composition of the main inflow (Table 2), suggesting that Lake Emanda is predominantly in the ice-free season fed by meteoric waters, i.e. precipitation with contribution of riverine input.

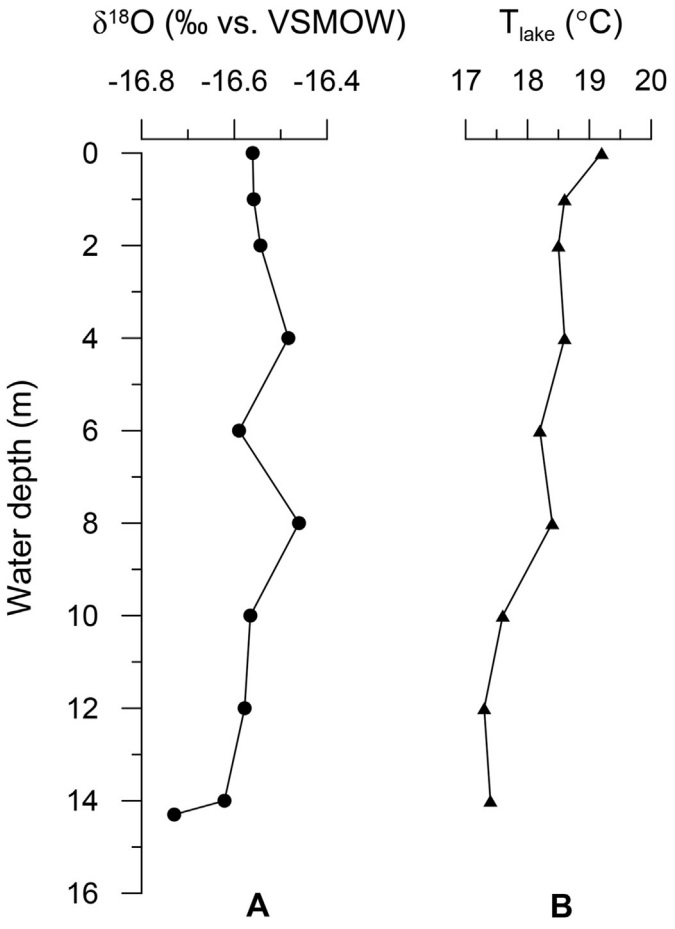

Fig. 9. Lake Emanda water depth profiles sampled at the Co1412 coring site in August 2017: (A) oxygen isotope and (B) temperature.

5.2. Isotope fractionation and controls on $\delta^{18}O_{diatom}$

Changes in $\delta^{18}O_{diatom}$ values are coupled with variations in the temperature (T_{lake}) and isotope composition ($\delta^{18}O_{lake}$) of coexisting water during diatom formation (Labeyrie, 1974; Juillet-Leclerc and Labeyrie, 1987; Leng and Barker, 2006; Dodd and Sharp, 2010).

The surface mean Lake Emanda $\delta^{18}O_{diatom}$ = +21.5‰ combined with the present day $\delta^{18}O_{lake}$ varying between −16.7 and −16.4‰ (mean: −16.5‰) indicates a reasonable water–silica isotope fractionation factors $\alpha_{(SiO2\text{-}H2O)} = (1000 + \delta^{18}O_{diatom})/(1000 + \delta^{18}O_{lake})$ (Juillet-Leclerc and Labeyrie, 1987) between 1.0385 and 1.0389 (mean: 1.0386). The established isotope fractionation correlation between fossil diatom silica and water (Juillet-Leclerc and Labeyrie, 1987):

$$1000 \cdots \ln\alpha_{(SiO2-H2O)} = 3.26 \cdots 10^6/T^2 + 0.45 \quad (2)$$

yields a calculated T_{lake} between 20.9 and 22.1 °C (mean: 21.8 °C) for diatom bloom, suggesting that the Lake Emanda $\delta^{18}O_{diatom}$ may properly reflect the summer $\delta^{18}O_{lake}$.

Using equation (2), the present day $\delta^{18}O_{lake}$ and T_{lake} measured during the field campaign between 17 and 21 °C, we calculated the expected $\delta^{18}O_{diatom}$ between +21.7 and + 22.8‰ (mean $\delta^{18}O_{diatom}$ = +22.3‰) for recent Lake Emanda conditions. These values are close to the measured surface mean $\delta^{18}O_{diatom}$ demonstrating the general applicability of diatom oxygen isotope signal for palaeoreconstructions in the study region.

Assuming that T_{lake} is the major control for Lake Emanda $\delta^{18}O_{diatom}$ and considering a lacustrine $\delta^{18}O_{diatom}/T_{lake}$ coefficient of −0.2‰/°C (Dodd and Sharp, 2010), a gradual depletion of ~4.9‰ in the record since the Early Holocene would imply a theoretical increase of 24 °C in the summer T_{lake}. Because this scenario is the opposite of known climate development in northeastern Siberia (Müller et al., 2009; Nazarova et al., 2013; Biskaborn et al., 2016), and as well as the modern water temperature in Lake Emanda reaches not more than 21 °C by mid-August, a change of 24 °C during the short summer period in the colder, eastern slope of the Verkhoyansk Mountain Range is unrealistic. Consequently, we assume a minor relevance of the T_{lake} changes for the Lake Emanda $\delta^{18}O_{diatom}$ trend. Therefore, the shifts in $\delta^{18}O_{diatom}$ are assumed to reflect changes in $\delta^{18}O_{lake}$ connected to variations in $\delta^{18}O_{prec}$ and/or the hydrological conditions in the lake and catchment as postulated by numerous previous studies (e.g. Kostrova et al., 2013; 2014; 2019; Meyer et al., 2015a; Cartier et al., 2019; Harding et al., 2020).

Variations in $\delta^{18}O_{prec}$ are predominantly defined by local condensation temperatures (T_{air}) (Dansgaard, 1964) and by the origin and history of air-mass trajectories (Merlivat and Jouzel, 1979; Kurita, 2011). The linear correlation between modelled mean monthly $\delta^{18}O_{prec}$ (Bowen, 2020) and mean monthly T_{air} derived from the monthly climate means data sets provided by the Hydrometcenter of Russia (available at http://old.meteoinfo.ru/climatcities) yields annual $\delta^{18}O_{prec}/T_{air}$ coefficient of +0.43‰/°C (n = 12; R^2 = 0.98) for the Iema meteorological station (Figs. 1B and 2). This coefficient is close to +0.37‰/°C (n = 12; R^2 = 0.97; GNIP database; 1969–2000 CE; IAEA/WMO, 2020) for Yakutsk (95 m a.s.l) located ~460 km to the southwest of Lake Emanda (Fig. 1). Due to the present annual amplitude of T_{air} at Lake Emanda (Fig. 2) being approximately three times higher than the annual T_{lake} range, T_{air} has a stronger effect on $\delta^{18}O_{lake}$ than T_{lake} and consequently, variations in Lake Emanda $\delta^{18}O_{diatom}$ are related to changes in T_{air} rather than to T_{lake}. Quantitative reconstructions revealed shifts in

mean annual T_{air} of 5–6 °C for the last ~13 cal ka BP in Central Yakutia (Fradkina et al., 2005). This would account for changes in ~1.2–1.4‰ in Lake Emanda $\delta^{18}O_{diatom}$ if we combine the $\delta^{18}O_{prec}/T_{air}$ and $\delta^{18}O_{diatom}/T_{lake}$ fractionation coefficients (Leng and Barker, 2006) assuming that these relationships are constant through the investigated period.

Variations in the relative contribution of the air masses of various origins to the local precipitation would change $\delta^{18}O_{lake}$ and accordingly $\delta^{18}O_{diatom}$. Presently, air masses varying in their origin from the North Atlantic in the west to the North Pacific in the east (Fig. 6A) combined in three main types supply moisture to the Lake Emanda region following well-established atmospheric circulation patterns over northeastern Siberia (Wiese, 1927; Cherdonova (Atlasova), 1993; Papina et al., 2017; Bonne et al., 2020). Among the three identified main directions of atmospheric moisture, the westerly air masses (Fig. 6B; cluster 1) prevail slightly over the south/southeast air masses (Fig. 6B; cluster 2), and together contribute about 75% of all regional moisture in the second half of the year. The remaining 25% of precipitation events indicate moisture pathways approaching Lake Emanda from the north (Fig. 6B; cluster 3). Precipitation delivered from the west is characterised by higher mean values ($\delta^{18}O_{prec} = -23.7$‰) as compared to moisture transported from the south/southeast ($\delta^{18}O_{prec} = -27.4$‰). Northern air masses include precipitation with the lowest mean values of $\delta^{18}O_{prec} = -33.4$‰. This is in good agreement with the recent findings (Papina et al., 2017; Bonne et al., 2020) about moisture sources for Central and northern Siberia. In general, if changes in air-mass prevalence occur through time, these may subsequently change $\delta^{18}O_{lake}$ and should be reflected in the $\delta^{18}O_{diatom}$ record. A greater contribution from the northern and/or the south/southeast air masses would shift regional $\delta^{18}O_{prec}$ and accordingly Lake Emanda $\delta^{18}O_{lake}$ and $\delta^{18}O_{diatom}$ to more negative values as compared to the moisture coming from the west. Additionally, precipitation intermittency i.e. prevalent winter precipitation in the regional water balance would also lead to lower $\delta^{18}O_{diatom}$, whereas strengthening of summer cyclonic activity implies a shift in $\delta^{18}O_{diatom}$ towards higher values.

Moreover, evaporation, which is in the study region up to four–seven times higher than the amount of precipitation during very dry seasons (Gavrilova, 1973), would cause significant enrichment of the lake water and result in a strong increase in $\delta^{18}O_{diatom}$. Lake Emanda is located close to the cold pole of the NH, also known as a very dry region (Ashastina et al., 2018). Ice-wedge water isotope records from the nearby Batagay/Adicha area were interpreted as persistently cold winter temperatures in the regional context (Opel et al., 2019). A more enduring lake ice cover in colder climate conditions would reduce evaporation effects and lead to lower $\delta^{18}O_{diatom}$. In addition, an increase in T_{air} may cause enhanced melting of the mountain snow and ice and thawing in the active layer of the permafrost in the Lake Emanda catchment providing an increased influx of depleted meltwater to the lake resulting in decline in $\delta^{18}O_{diatom}$.

Despite uncertainties in the development of isotope signal through time, we suggest that the changes in Lake Emanda $\delta^{18}O_{lake}$ and, as a consequence, $\delta^{18}O_{diatom}$ are mainly driven by changes in: (1) $\delta^{18}O_{prec}$ either related to variations in T_{air} or/and relative contribution of moisture sources, (2) varying evaporative effects and (3) meltwater supply.

5.3. Temporal development of diatom oxygen isotope and assemblage records in the local context

At Lake Emanda, a suitable aquatic habitat for diatoms established at ~13.2 cal ka BP. The freshwater planktonic *Cyclotella iris* preferring cold oligotrophic conditions (Barinova et al., 2006) dominates the diatom assemblage through the core reaching a relative abundance of up to 85%.

Between ~13.2 and 11.7 cal ka BP, the $\delta^{18}O_{diatom}$ record is characterized by relatively low values of about +26.2‰ (Fig. 4A). Diatom assemblages are mainly represented by small benthic fragilarioid species *S. pinnata*, *S. venter* and *S. construens* known as late-glacial pioneering species (Haworth, 1975; 1976), and planktonic *C. iris* (Fig. 7). Substantial dominance of fragilariod taxa (70–75%), combined with low diatom concentrations ($4–18 \times 10^6$ valves g^{-1}) and relatively low total organic carbon (TOC; 2–4%; Baumer et al., 2020) denote a cold boreal lake system with long severe winters and an extended ice-covered period (Biskaborn et al., 2012; 2016). *C. iris* indicates that the water depth was already high enough to allow for the growth of planktonic species.

A shift of ~2‰ towards higher values appears in the $\delta^{18}O_{diatom}$ record at 11.7–11.0 cal ka BP (Fig. 4A) and almost synchronously with the increases in the diatom species richness and Hill's N2 diversity index (Fig. 4D and E). Strong dominance of planktonic species (80–85%; Fig. 7) can be related to greater water transparency and longer ice-free periods, suggesting a general warming (Biskaborn et al., 2012). This could be indicative for an increase in water levels and/or reduced mixing of the water column. At the same time, a sharp twofold increase (from 4 to 8%) in TOC detected in the same core (Baumer et al., 2020) indicates a peak in productivity linked with an overall increase in air temperature.

Between ~11.0 and 9.7 cal ka BP, a stepwise decline in $\delta^{18}O_{diatom}$ values accompanied by a rise of TDC (Fig. 4C) in parallel with major changes in the diatom assemblage (Fig. 7) may reflect a meltwater input in response to further climate warming (Baumer et al., 2020). At this time, *L. bodanica* becomes the second dominant planktonic species potentially pointing to an increase in water level as well as changes in nutrient supply (Saros and Anderson, 2015). A possible indication that *L. bodanica* was favoured by an input of melt water is the restriction of this species to a rather short time period (Fig. 7) during the initial regional warming. A general increase of benthic taxa such as *Navicula* spp. and *C. cocconeiformis* at the same time indicates a gradual establishment of habitats for a broader range of diatom ecotypes during the Early Holocene warming (Biskaborn et al., 2012).

Between ~9.7 and 8.1 cal ka BP, $\delta^{18}O_{diatom}$ values exhibit sharp variations of ~1–1.5‰ every 200–300 yrs (Fig. 4A). In contrast, the diatom assemblage record demonstrates less variability most likely due to lower temporal resolution (Fig. 7). Strong fluctuations in $\delta^{18}O_{diatom}$ are overprinted by a general decrease of the isotope signal accompanied by an increase in TDC and species richness (Fig. 4C and D). *L. bodanica* is still present while *Aulacoseira* species occur in higher percentages (>30%; Fig. 7). *A. ambigua,* that is reported as an alkaliphilic species that requires sufficient nutrient input (Barinova et al., 2011), would benefit from increased silica supply. At the same time, the shift from *Cyclotella* to *Aulacoseira* and increased planktonic taxa indicate a deepening lake habitat with longer ice-free seasons enabling sufficient water turbulence needed for the growth of the highly silicified frustules of this taxon (Rühland et al., 2015). This indicates, that water turbulence and likely also increased river flow facilitated nutrient regeneration in the lake during that time.

In the interval ~8.1–6.8 cal ka BP, two $\delta^{18}O_{diatom}$ maxima of +27.8 and + 27.5‰ separated by a pronounced minimum of +24.5‰ are displayed (Fig. 4A). At this time, TDC, species richness and Hill's N2 exhibit their high values (Fig. 4C, D and E). An increase of these diatom indices may be interpreted as climate warming in the catchment leading to increased soil formation and weathering (Schleusner et al., 2015). Catchment-derived nutrient supply led to increased diatom productivity and, thus, TDC (Fig. 4C). High abundance of *A. ambigua* over this period can be interpreted

as shortening of the ice-covered period due to a general warming of winters (Meyer et al., 2015b). Given the combined isotope and taxonomical diatom data, we can infer this period as a Mid Holocene Thermal Maximum (HTM). Both assemblage composition and isotope records suggest that the HTM occurred ~2–3 thousand years later than it was reconstructed for Lake Emanda from the sedimentological and geochemical data (Baumer et al., 2020). Diatoms and their isotope composition are directly linked with local changes in the aquatic system and hydrology and react on temperature change, whereas the sedimentary proxies rather reflect an input from the catchment.

After ~6.8 cal ka BP, relatively constant $\delta^{18}O_{diatom}$ values around +24.8 ± 0.3‰ suddenly drop to +23.2‰ at ~5.2 cal ka BP (Fig. 4A). At the same time, TDC, species richness and Hill's N2 diversity gradually decrease reaching low peak values (Fig. 4C, D and E). The diatom assemblage demonstrates a notable increase of naviculoid species such as *S. pupula* and several *Pinnularia* and *Amphora* taxa and a steady decrease of planktonic forms with the disappearance of *A. ambigua* at ~6.0–5.8 cal ka BP (Fig. 7). The decrease of planktonic taxa is, though, not mirrored in the gradual increase of PC2 sample scores. The resilience of the diatom assemblage as an ecosystem is supported by its response to the strong regional cooling at ~5.2 cal ka BP (Fradkina et al., 2005) suggested by $\delta^{18}O_{diatom}$ values (Fig. 4A). Here, only TDC and species richness are decreasing without strong compositional changes (Fig. 4C and D).

After ~5.0 cal ka BP, $\delta^{18}O_{diatom}$ values exhibit a pronounced decline with visible minima at ~3.1–3.0, 1.3, and 0.4 cal ka BP (Fig. 4A). Statistical changes occur at ~3.3–2.0 cal ka BP, when TDC reach its maximum, then suddenly drop to very low amounts (Fig. 4C). At the same time, a shift between planktonic species from *P. tripartita* (oligotrophic) to *P. ocellata* (mesotrophic) and a distinct decrease in *P. nodosa* (oligotrophic) (Fig. 7) can be interpreted as an increase in nutrient supply from the catchment. After 2.0 cal ka BP, increasing Hill's N2 diversity (Fig. 4E) is related to changes and minor increases in benthic species, while the strong increase of PC2 can be related to the sudden increase of *P. tripartita* in the surface sample as this species contributes strongly to the variance shown in the biplot (Figs. 4F, 7 and 8).

The $\delta^{18}O_{diatom}$ record correlates positively with the time series of PCA 1 scores ($R^2 = 0.76$, $p < 0.001$), while a statistically not significant correlation was found with PCA 2 scores ($R^2 = 0.002$, $p = 0.88$), which suggests that the diatom isotope composition and diatom assemblages compared over the full time series record responded differently to climate-driven shifts. Therefore, we can assume that species effects did not affect the isotopic signal.

5.4. Regional palaeoenvironment

The Lake Emanda $\delta^{18}O_{diatom}$ record documents a pronounced temporal variability consistent with the regional climate for the past ~13.2 cal ka BP.

Between ~13.2 and 11.7 ka BP, the $\delta^{18}O_{diatom}$ values remain relatively stable varying around +26.2‰ (Fig. 10A), despite a rather weak chronological control of the lateglacial samples. Short-term warm and cold phases known from the regional pollen-based temperature reconstructions (Anderson et al., 2002; Fradkina et al., 2005; Müller et al., 2009; Werner et al., 2010) are not clearly reflected in the $\delta^{18}O_{diatom}$ record. The overall level of $\delta^{18}O_{diatom}$ values in the rather cold and dry Younger Dryas interval (~12.9–11.7 cal ka BP) is comparable to those in the warmer Allerød (~13.2–12.9 cal ka BP) and seems to not directly correspond to air temperature changes (Fradkina et al., 2005; Müller et al., 2009), since a general lowering of T_{air} would lead to lower $\delta^{18}O_{lake}$ and, thus, $\delta^{18}O_{diatom}$. However, the $\delta^{18}O_{diatom}$ record has not revealed a significantly lower diatom isotope signal for the Younger Dryas (with +25.9‰) compared to the Holocene average (+25.2‰). The relatively high $\delta^{18}O_{diatom}$ values during the comparatively cold and dry Younger Dryas (Fig. 10A) are most likely caused by increased evaporation rates likely playing a major role in controlling $\delta^{18}O_{lake}$. Hence, under arid Younger Dryas conditions (Andreev et al., 1997; Fradkina et al., 2005; Andreev and Tarasov, 2013), evaporation could significantly exceed the amount of precipitation (Gavrilova, 1973; Müller et al., 2009) and partly compensate the effect of lower T_{air} on $\delta^{18}O_{diatom}$ at this time. A reduced overall level of summer precipitation is further supported by a stronger Siberian High during the Younger Dryas (Fig. 10E; Mayewski et al., 2004), the region's dominant pressure system, as reflected in the Greenland K^+ record (cit), blocking the moisture. Less precipitation would lead to a reduction of isotopically light riverine input from higher altitudes of the catchment, and hence to further isotope enrichment of the lake water. Moreover, a cold and arid Younger Dryas could induce a more persistent lake ice cover and, thus, reducing evaporation. In summary, despite the known very dry and cold conditions in the Younger Dryas, the $\delta^{18}O_{diatom}$ values are not extreme likely due to the discussed counter-balancing hydrological and climatic effects.

An abrupt increase in the $\delta^{18}O_{diatom}$ values at ~11.7–11.5 cal ka BP (Fig. 10A) could be associated with the transition from rather cold/dry lateglacial conditions to a relatively warm/humid Holocene climate. This is consistent with the definition of the Holocene onset in the northern part of Yakutia (Andreev et al., 2011), in the Yana Highlands (Ashastina et al., 2017; Baumer et al., 2020), and Chukotka (Swann et al., 2010). However, this shift in the $\delta^{18}O_{diatom}$ record is slightly earlier than reconstructed from numerous regional pollen records at ~11.5–11.2 cal ka BP (Anderson et al., 2002; Fradkina et al., 2005; Müller et al., 2009; Andreev and Tarasov, 2013), when a sharp increase in forest vegetation occurred accompanied by an increase of the mean annual air temperatures by 3–4 °C and of precipitation levels by 100–120 mm (Fradkina et al., 2005; Tarasov et al., 2013). Moreover, the weakened Siberian High (Fig. 10) implies the possibility of enhanced moisture supply reaching the Lake Emanda region. The relatively high $\delta^{18}O_{diatom}$ values could be indicative for prevailing westerly air masses entering the region, i.e. after the decay of the Eurasian Ice Sheet.

A stepwise decrease in the lake $\delta^{18}O_{diatom}$ values from +27.4‰ at 11.0 cal ka BP to +25.9‰ at 9.7 cal ka BP (Fig. 10A) is accompanied by generally increasing precipitation rates and rising air temperatures at the beginning of the Holocene (Fradkina et al., 2005) and could reflect increased meltwater input from the hinterland as a result of overall warming (Anderson et al., 2002; Müller et al., 2009; Biskaborn et al., 2012; 2016). A similar phenomenon with decreasing $\delta^{18}O_{diatom}$ due to an increased influx of melt water from higher altitudes in the Early Holocene was described for Lake Kotokel in southern Siberia (Fig. 10C; Kostrova et al., 2013). Relatively high $\delta^{18}O_{diatom}$ values of ~+26.6‰ at this time are likely associated with higher evaporation levels induced by the summer insolation maximum (Fig. 10G; Berger and Loutre, 1991; Werner et al., 2010). Evaporation/sublimation cannot be ruled out in winter neither, when from an open snow surface, mass loss can reach, on average, ~16% of the total snow storage (Fedorov et al., 2014).

The character of the $\delta^{18}O_{diatom}$ record between ~8.1 and 5.5 cal ka BP is in line with a postglacial climate warming in northeastern Siberia at ~9–5.1 cal ka BP as inferred from stable isotope composition of ground ice in the Verkhoyansk foreland (Popp et al., 2006). Lake Emanda shows two Holocene $\delta^{18}O_{diatom}$ maxima between ~7.9 and 7.0 cal ka BP (Fig. 10A), consistent with a summer temperature maximum inferred from the regional pollen reconstructions

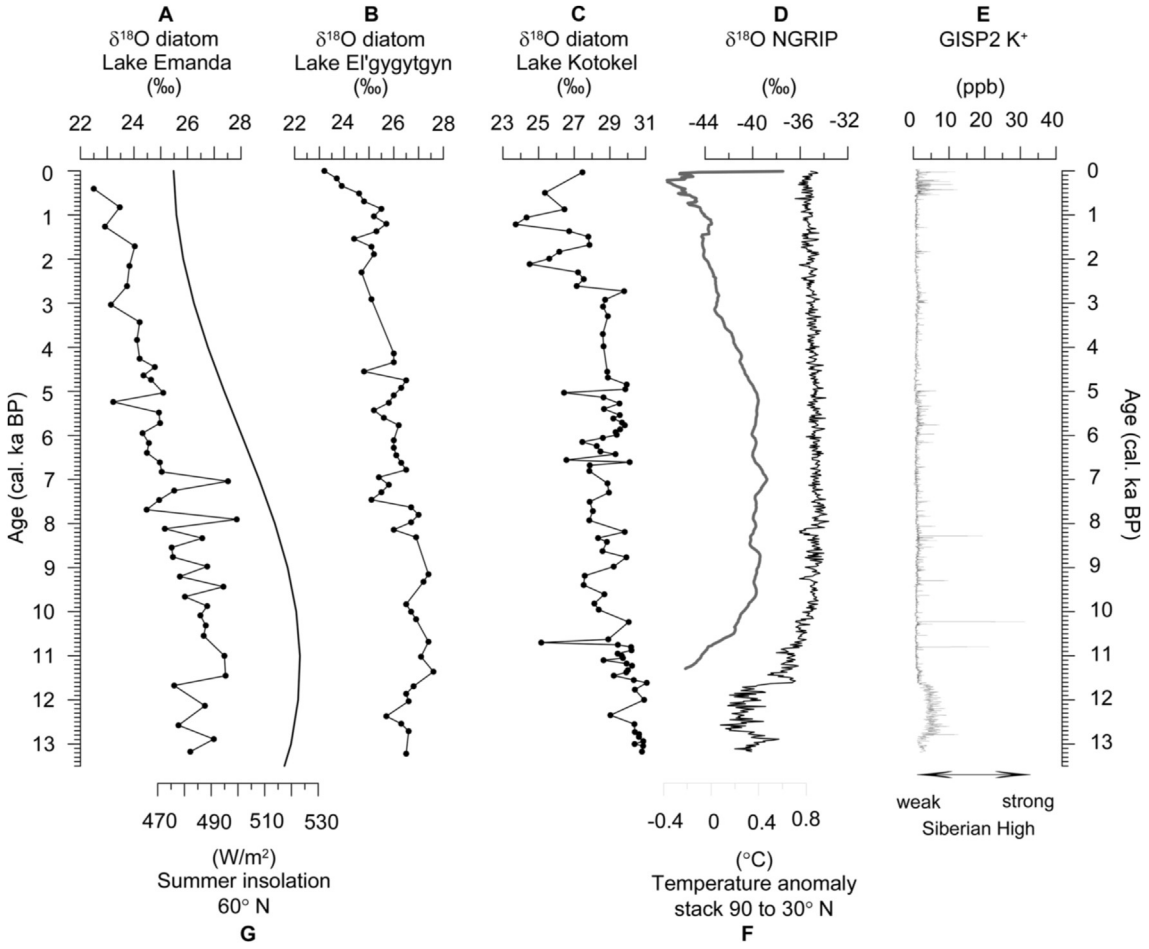

Fig. 10. (A) Oxygen isotope composition of diatoms from Lake Emanda compared to other North Hemispheric (NH) climate reconstructions such as (B) oxygen isotope composition of diatoms from Lake El'gygytgyn, Chukotka (Swann et al., 2010), (C) oxygen isotope composition of diatoms from Lake Kotokel, southern Siberia (Kostrova et al., 2013; 2014), (D) NGRIP oxygen isotope record from Greenland ice (Svensson et al., 2008) as indicator of the NH air temperature, (E) GISP2 potassium (K^+) ion record as indicator for the Siberian High intensity (Mayewski et al., 2004), (G) the NH summer insolation at 60° N (Berger and Loutre, 1991), and (F) the NH temperature anomaly (stack 90 to 30° N; Marcott et al., 2013).

(Klemm et al., 2013; Biskaborn et al., 2016). In response to climate warming and degradation of the permafrost layer, boreal forest communities started invading the area around the Verkhoyansk Range since ~7.0 cal ka BP (Anderson et al., 2002; Müller et al., 2009; Werner et al., 2010). At the same time, permafrost thaw and extensive thermokarst basin development took place in the region (Ulrich et al., 2019). Thus, a relatively low $\delta^{18}O_{diatom}$ between ~7.0 and 5.5 cal ka BP could suggest melt water release from the hinterland as well as from permafrost thaw (Opel et al., 2019) as a reaction to high T_{air}, but could also indicate a moisture source change towards less westerly, but more east- or northbound precipitation with enhanced strength of the Siberian High (Fig. 10E).

The $\delta^{18}O_{diatom}$ record shows a minimum at 5.2 cal ka BP (Fig. 10A), which can be attributed to an abrupt climate event (Roland et al., 2015). As recorded in the regional palaeoclimate archives, this event is traced by a significant decrease of tree pollen (Fradkina et al., 2005; Biskaborn et al., 2016), associated with lower than modern annual air temperatures and precipitation by 2 °C and 25 mm, respectively (Fradkina et al., 2005).

After ~5.0 cal ka BP, a continuous decline of ~2.5‰ in $\delta^{18}O_{diatom}$ values can be basically attributed to regional Neoglacial cooling, which started at ~5.1 cal ka BP (Popp et al., 2006; Klemm et al., 2013; 2016; Biskaborn et al., 2016). Palaeoclimate reconstructions based on chironomid data exhibit lower than present mean July air temperatures during the Late Holocene in the region (Nazarova et al., 2013). Distinct minima superimposed on the overall cooling trend are registered in the $\delta^{18}O_{diatom}$ record at ~3.0 and ~1.3 cal ka BP and correspond to significant regional cooling when average annual air temperatures were lower than modern by ~1.5 °C (Fradkina et al., 2005). The widespread cooling induced an extensive permafrost aggradation and a significant decrease of thermokarst activity after ~1.5 cal ka BP (Ulrich et al., 2019). A general cooling related to the gradual decrease of summer insolation reduced the evaporation effects on Yakutian lakes (Wetterich et al., 2008; Biskaborn et al., 2012; Klemm et al., 2013) and, thus, may have forced a decrease of $\delta^{18}O_{lake}$ in the Late Holocene. Additionally, a stronger Siberian High (Fig. 10E) could have been accompanied by the reduction of westerly moisture supply to the region.

Additionally, the (yet unpublished) Lake Emanda pollen record is indicative for environmental changes in the region and yields high resolution data on local plant communities and their dynamics. The continuous decrease in $\delta^{18}O_{diatom}$ over the Holocene is in line with a simultaneous decrease in *Alnus* pollen (A. Andreev, pers. comm.) which has been identified as a good indicator for local summer temperatures (Klemm et al., 2013).

5.5. Extra-regional comparison

The overall trend in the Lake Emanda $\delta^{18}O_{diatom}$ record (Fig. 10A) clearly follows the summer solar insolation at 60°N (Fig. 10G;

Berger and Loutre, 1991), suggesting a sensitivity of the diatom isotope signal to changes in solar radiation (or to a variable sensitive to insolation, such as lake ice cover duration) and, therefore, a good response to insolation-induced temperature changes. Moreover, the $\delta^{18}O_{diatom}$ record demonstrates notable similarity with the NH air temperatures as archived in the Greenland ice core (NGRIP; Fig. 10D; Svensson et al., 2008) and the stacked temperature anomaly (Fig. 10F; Marcott et al., 2013). In particular, short-term $\delta^{18}O_{diatom}$ fluctuations between ~13.2 and 11.7 cal ka BP are in line with shifts in the NGRIP $\delta^{18}O$ record and indicate an almost synchronous response of the lake ecosystem to global climate changes. In addition, an obvious shift in the $\delta^{18}O_{diatom}$ towards higher values at ~11.7–11.5 cal ka BP is also detected in the NGRIP record and reflects a reaction to a progressive climate warming (Kaufman et al., 2020) and indicates the almost contemporaneous onset of the Holocene across Eurasia.

Moreover, the Lake Emanda $\delta^{18}O_{diatom}$ record demonstrates consistency with many other climate reconstructions of the NH (Wanner et al., 2008; Miller et al., 2010). Especially, the pattern of the Lake Emanda $\delta^{18}O_{diatom}$ record is close to that obtained from Lake El'gygytgyn in Chukotka (Figs. 1A and 10A and B; Swann et al., 2010; Chapligin et al., 2012b). The similarity is striking with a continuous decreasing trend over the complete Holocene, overprinted by higher Mid Holocene internal variability and a Late Holocene absolute minimum (Fig. 10A and B). Both lakes are situated east of the Verkhoyansk Mountain Range (Fig. 1A), an orographic barrier for westerly precipitation, and receive large parts of their moisture from the east (own data; Papina et al., 2017; Shestakova et al., 2020). The lakes have rather small, locally confined catchments, presently no glaciers in the hinterland, and only one main outflow. But they also show general differences in their lake characteristics and hydrology, with Lake Emanda being shallower (thus more prone for evaporative effects), smaller in lake surface, and likely with shorter residence times (decadal vs. centennial time scales). The general variability ($\Delta^{18}O = 5.3‰$) is higher in the Lake Emanda $\delta^{18}O_{diatom}$ record, as compared to Lake El'gygytgyn ($\Delta^{18}O = 4.4‰$), which is likely related to the beforementioned aspects. However, the differences between both records are smaller than the hydrological differences would suggest, with clear evaporation effects documented at Lake Emanda and a clear correlation with mean annual air temperatures at Lake El'gygytgyn (Chapligin et al., 2012b). We, therefore, assume that both lakes are subject to the same external forcing, at least throughout the Holocene, and belong to the same larger hydrological province.

However, both records as well as that of Lake Kotokel in southern Siberia (Figs. 1A and 10C; Kostrova et al., 2013; 2014) generally demonstrate high $\delta^{18}O_{diatom}$ values in the Early and Middle Holocene, which could be either interpreted as HTM (Swann et al., 2010; Chapligin et al., 2012b) or enhanced evaporation in relatively dry conditions (Kostrova et al., 2013). The Lake Emanda record reveals two $\delta^{18}O_{diatom}$ maxima at ~7.9 and 7.0 cal ka BP (Fig. 10A), roughly consistent with the summer temperature maximum inferred from diatom assemblages (Chapter 5.3) and other regional proxy sources (Biskaborn et al., 2012; 2016). These maxima could either indicate a Mid HTM as demonstrated above or be interpreted as short-term interruptions of a general decrease in $\delta^{18}O_{diatom}$ after the Early Holocene. In this context, relatively high Lake Emanda $\delta^{18}O_{diatom}$ at 11.7–9.0 cal ka BP could be interpreted as an Early HTM, which is also supported by maximum TOC values (Baumer et al., 2020). An Early HTM has been also reconstructed based on Lake El'gygytgyn $\delta^{18}O_{diatom}$ data at 11.4–7.6 cal ka BP (Fig. 10B; Swann et al., 2010; Chapligin et al., 2012b) and confirmed by Kaufman et al. (2004) for several locations of eastern Beringia in a hemispheric proxy compilation.

As reconstructed from numerous temperature-sensitive proxy records worldwide (Marcott et al., 2013; Kaufman et al., 2004; 2020), a pronounced Holocene cooling is expressed in all discussed $\delta^{18}O_{diatom}$ records by the overall depletion ending with a visible minimum at ~0.8–0.4 cal ka BP (Fig. 10) likely corresponding to the Little Ice Age (LIA; Fig. 10F; Marcott et al., 2013), and accompanied by generally reduced evaporation and more persistent lake ice cover (Swann et al., 2010; Kostrova et al., 2013).

Additionally, air-mass changes are considered to be driving the Holocene climate variations. The general trend in the Lake Emanda $\delta^{18}O_{diatom}$ record through the Holocene could also partly be attributed to varying precipitation sources. Generally, the long-distance transport from the west has to pass the orographic barrier of the Verkhoyansk Mountain Range, and would be expected to be isotopically more depleted than more proximal moisture from the east. However, this is not confirmed by our studies of modern moisture origin and $\delta^{18}O_{prec}$, which show the western cluster 1 to be more enriched than precipitation from the east (cluster 2), at least for the year 2017. Hence, in this line of argument, a greater proportion of moisture delivered from western sources could have caused generally higher $\delta^{18}O_{diatom}$ values in the Early Holocene, and lower Late Holocene $\delta^{18}O_{diatom}$ be associated with more northerly or eastbound moisture. However, recent studies (Rudaya et al., 2009; Kleinen et al., 2011; Kostrova et al., 2013; Kobe et al., 2020; Harding et al., 2020) have demonstrated that westerly moisture transport was weaker in the middle latitudes of Eurasia until mid-Holocene, while south-easterly derived moisture played a more significant role. If such a scenario is adopted to the more northerly Lake Emanda, then a decreasing $\delta^{18}O_{diatom}$ over the Holocene should be accompanied by higher amounts of precipitation originating from the west and/or north, and our observations from 2017 suggest an important recent contribution of Arctic moisture. This is in line with a currently reduced sea-ice cover in an amplified warming Arctic.

6. Conclusions

The diatom oxygen isotope and assemblage records from the Co1412 core of Lake Emanda are complemented by the recent contemporary isotope hydrology and modelled atmospheric circulation patterns. The data provide important information on the environmental, hydrological and climate dynamics in northeastern Siberia during the lateglacial transition and the complete Holocene. Over the last ~13.2 cal ka, the lake existed as a relatively cold and well-mixed freshwater system. The surface $\delta^{18}O_{diatom} = +21.5‰$ correlates well with present-day lake water isotopes (mean $\delta^{18}O_{lake} = -16.5‰$), indicating a water–silica isotope fractionation ($\alpha = 1.0386$) at a calculated T_{lake} of 21.8 °C. This properly reflects summer blooming conditions and demonstrates the applicability of diatom oxygen isotope signal for summer-based palaeoreconstructions in the region. Nevertheless, the diatom isotope variability in Lake Emanda is controlled by changes in $\delta^{18}O_{lake}$ rather than changes in T_{lake}, and associated with evaporation effects. A decrease in $\delta^{18}O_{diatom}$ in the Early Holocene accompanied by an increasing diatom concentration could be linked to meltwater release from the hinterland around Lake Emanda.

The Lake Emanda $\delta^{18}O_{diatom}$ trend follows a decrease in summer insolation, in line with the regional and the NH temperature history, demonstrating a good response of the isotope signal to insolation-driven temperature changes. The onset of the Holocene is marked in the isotope record by an obvious shift of ~2‰ at 11.7–11.5 cal ka BP, accompanied by significant changes in diatom assemblages. Comparatively high $\delta^{18}O_{diatom}$ values around +26.6‰ are in line with the summer insolation maximum, suggest a relatively warm Early Holocene and are associated with and/or

superimposed by enhanced evaporation. Absolute maximum $\delta^{18}O_{diatom}$ values of +27.7‰ at ~7.9–7.0 cal ka BP consistent with high values of diatom indices point to a Mid HTM. Apparent minima both in $\delta^{18}O_{diatom}$ values and diatom indices provide evidence for a pronounced (Neoglacial) cooling event at ~5.2 cal ka BP. The absolute minimum in the Lake Emanda $\delta^{18}O_{diatom}$ record of +22.5‰ at 0.4 cal ka BP corresponds to the LIA and associated with colder T_{air}, a more persistent lake ice cover and reduced evaporation. The striking similarity of the Lake Emanda and El'gygytgyn $\delta^{18}O_{diatom}$ records despite obvious hydrological differences points to a common regional climate signal.

The study of the modern moisture origin and stable isotope characteristics of atmospheric precipitation at Lake Emanda revealed rather equivalent roles of westerly, North Atlantic and easterly, North Pacific moisture transported to the study region throughout the year.

Author contributions

S. Kostrova, H. Meyer provided the diatom oxygen and water isotope data; B. Biskaborn, L. Pestryakova provided the diatom taxonomy data; F. Fernandoy provided HYSPLIT modelling; M. Lenz provided the lithological data and age-depth model. All co-authors contributed to the discussion and interpretation of the data and the writing of the manuscript.

Data availability statement

Data are available via the Pangaea database (www.pangaea.de).

Declaration of competing interest

The authors declare that they have no known competing financial interests or personal relationships that could have appeared to influence the work reported in this paper.

Acknowledgements

This study was performed as part of the 'PLOT–Paleolimnological Transect' project funded by the German Federal Ministry of Education and Research; Germany (BMBF; grant 03G0859). We appreciate Prof. Dmitry Bolshiyanov from the Arctic and Antarctic Research Institute in St. Petersburg for his help during the field campaign. We thank Ilona Burghardt from the German Research Center for Geosciences (GFZ) in Potsdam for the EDS analyses. Mikaela Weiner is acknowledged for technical support during sample preparation and isotope measurements at the AWI Potsdam stable isotope facility. Research of Dr. Svetlana Kostrova contributes to the State Research Program of IGC SB RAS 0284-2021-0003. Research of Dr. Luidmila Pestryakova has been partly supported by the Russian Foundation for Basic Research; Russia (RFBR; grant 18-45-140053 r_a) and the Ministry of Science and Higher Education of the Russian Federation; Russia (grant FSRG-2020-0019). We are grateful to Prof. Anson W. Mackay and an anonymous reviewer for their helpful and constructive comments on the manuscript.

References

Aas, K.S., Martin, L., Nitzbon, J., Langer, M., Boike, J., Lee, H., Berntsen, T.K., Westermann, S., 2019. Thaw processes in ice-rich permafrost landscapes represented with laterally coupled tiles in a land surface model. Cryosphere 13, 591–609. https://doi.org/10.5194/tc-13-591-2019.

ACIA, 2005. Arctic Climate Impact Assessment. Cambridge University Press, Cambridge.

Anderson, P.M., Lozhkin, A.V., Brubaker, L.B., 2002. Implications of a 24,000-Yr palynological record for a Younger Dryas cooling and for boreal forest development in northeastern Siberia. Quat. Res. 57, 325–333. https://doi.org/10.1006/qres.2002.2321.

Andreev, A.A., Klimanov, V.A., Sulerzhitsky, L.D., 1997. Younger Dryas pollen records from central and southern Yakutia. Quat. Int. 41–42, 111–117. https://doi.org/10.1016/S1040-6182(96)00042-0.

Andreev, A.A., Schirrmeister, L., Tarasov, P.E., Ganopolski, A., Brovkin, V., Siegert, C., Wetterich, S., Hubberten, H.-W., 2011. Vegetation and climate history in the Laptev sea region (arctic Siberia) during late Quaternary inferred from pollen records. Quat. Sci. Rev. 30, 2182–2199. https://doi.org/10.1016/j.quascirev.2010.12.026.

Andreev, A.A., Tarasov, P.E., 2013. Northern Asia. In: Elias, S.A. (Ed.), The Encyclopedia of Quaternary Science, vol. 4. Elsevier, Amsterdam, pp. 164–172.

Ashastina, K., Kuzmina, S., Rudaya, N., Troeva, E., Schoch, W.H., Römermann, C., Reinecke, J., Otte, V., Savvinov, G., Wesche, K., Kienast, F., 2018. Woodlands and steppes: Pleistocene vegetation in Yakutia's most continental part recorded in the Batagay permafrost sequence. Quat. Sci. Rev. 196, 38–61. https://doi.org/10.1016/j.quascirev.2018.07.032.

Ashastina, K., Schirrmeister, L., Fuchs, M., Kienast, F., 2017. Palaeoclimate characteristics in interior Siberia of MIS 6–2: first insights from the Batagay permafrost mega-thaw slump in the Yana Highlands. Clim. Past 13, 795–818. https://doi.org/10.5194/cp-13-795-2017.

Astakhov, V.I., 2018. Late Quaternary glaciation of the northern Urals: a review and new observations. Boreas 47, 379–389. https://doi.org/10.1111/bor.12278.

Bailey, H.L., Kaufman, D.S., Sloane, H.J., Hubbard, A.L., Henderson, A.C., Leng, M.J., Meyer, H., Welker, J.M., 2018. Holocene atmospheric circulation in the central North Pacific: a new terrestrial diatom and $\delta^{18}O$ dataset from the Aleutian Islands. Quat. Sci. Rev. 194, 27–38. https://doi.org/10.1016/j.quascirev.2018.06.027.

Barinova, S., Nevo, E., Bragina, T., 2011. Ecological assessment of wetland ecosystems of northern Kazakhstan on the basis of hydrochemistry and algal biodiversity. Acta Bot. Croat. 70 (2), 215–244.

Barinova, S.S., Medvedeva, L.A., Anisimova, O.V., 2006. Diversity of Algal Indicators in the Environmental Assessment. Pilies Studio. Tel Aviv. (in Russian).

Baumer, M.M., Wagner, B., Meyer, H., Leicher, N., Lenz, M., Fedorov, G., Pestryakova, L.A., Melles, M., 2020. Climatic and environmental changes in the Yana Highlands of north-eastern Siberia over the last c. 57 000 years, derived from a sediment core from Lake Emanda. Boreas. https://doi.org/10.1111/bor.12476.

Berger, A., Loutre, M.F., 1991. Insolation values for the climate of the last 10 million years. Quat. Sci. Rev. 10, 297–317. https://doi.org/10.1016/0277-3791(91)90033-Q.

Birks, H.J.B., 2010. Numerical methods for the analysis of diatom assemblage data. In: Smol, J.P., Stoermer, E.F. (Eds.), The Diatoms: Applications for the Environmental and Earth Science. Cambridge University Press, Cambridge, pp. 23–54.

Birks, H.J.B., Felde, V.A., Bjune, A.E., Grytnes, J.-A., Seppä, H., Giesecke, T., 2016. Does pollen-assemblage richness reflect floristic richness? A review of recent developments and future challenges. Rev. Palaeobot. Palynol. 228, 1–25. https://doi.org/10.1016/j.revpalbo.2015.12.011.

Biskaborn, B.K., Herzschuh, U., Bolshiyanov, D., Savelieva, L., Diekmann, B., 2012. Environmental variability in northeastern Siberia during the last ~13,300 yr inferred from lake diatoms and sediment–geochemical parameters. Palaeogeogr. Palaeoclimatol. Palaeoecol. 329–330, 22–36. https://doi.org/10.1016/j.palaeo.2012.02.003.

Biskaborn, B.K., Narancic, B., Stoof-Leichsenring, K.R., Pestryakova, L.A., Appleby, P.G., Piliposian, G.T., Diekmann, B., 2021. Effects of climate change and industrialization on Lake Bolshoe Toko, eastern Siberia. J. Paleolimnol. 65, 335–352. https://doi.org/10.1007/s10933-021-00175-z.

Biskaborn, B.K., Smith, S.L., Noetzli, J., Matthes, H., Vieira, G., Streletskiy, D.A., Schoeneich, P., Romanovsky, V.E., Lewkowicz, A.G., Abramov, A., Allard, M., Boike, J., Cable, W.L., Christiansen, H.H., Delaloye, R., Diekmann, B., Drozdov, D., Etzelmüller, B., Grosse, G., Guglielmin, M., Ingeman-Nielsen, T., Isaksen, K., Ishikawa, M., Johansson, M., Johannsson, H., Joo, A., Kaverin, D., Kholodov, A., Konstantinov, P., Kröger, T., Lambiel, C., Lanckman, J.-P., Luo, D., Malkova, G., Meiklejohn, I., Moskalenko, N., Oliva, M., Phillips, M., Ramos, M., Sannel, A.B.K., Sergeev, D., Seybold, C., Skryabin, P., Vasiliev, A., Wu, Q., Yoshikawa, K., Zheleznyak, M., Lantuit, H., 2019. Permafrost is warming at a global scale. Nat. Commun. 10, 264. https://doi.org/10.1038/s41467-018-08240-4.

Biskaborn, B.K., Subetto, D.A., Savelieva, L.A., Vakhrameeva, P.S., Hansche, A., Herzschuh, U., Klemm, J., Heinecke, L., Pestryakova, L.A., Meyer, H., Kuhn, G., Diekmann, B., 2016. Late Quaternary vegetation and lake system dynamics in northeastern Siberia: implications for seasonal climate variability. Quat. Sci. Rev. 147, 406–421. https://doi.org/10.1016/j.quascirev.2015.08.014.

Blaauw, M., Christen, J.A., 2011. Flexible paleoclimate age-depth models using an autoregressive gamma process. Bayesian Anal. 6, 457–474. https://doi.org/10.1214/11-BA618.

Boike, J., Grau, Th., Heim, B., Günther, F., Langer, M., Muster, S., Gouttevin, I., Lange, S., 2016. Satellite-derived changes in the permafrost landscape of central Yakutia, 2000–2011: wetting, drying, and fires. Global Planet. Change 139, 116–127. https://doi.org/10.1016/j.gloplacha.2016.01.001.

Bonne, J.-L., Meyer, H., Behrens, M., Boike, J., Kipfstuhl, S., Rabe, B., Schmidt, T., Schönicke, L., Steen-Larsen, H.C., Werner, M., 2020. Moisture origin as a driver of temporal variabilities of the water vapour isotopic composition in the Lena River Delta, Siberia. Atmos. Chem. Phys. 20, 10493–10511. https://doi.org/10.5194/acp-20-10493-2020.

Bowen, G.J., Revenaugh, J., 2003. Interpolating the isotopic composition of modern meteoric precipitation. Water Resour. Res. 39 (10), 1299. https://doi.org/

10.1029/2003WR002086.
Bowen, G.J., 2020. The Online Isotopes in Precipitation Calculator version 3.1. http://www.waterisotopes.org.
Cartier, R., Sylvestre, F., Paillès, C., Sonzogni, C., Couapel, M., Alexandre, A., Mazur, J.-C., Brisset, E., Miramont, C., Guiter, F., 2019. Diatom-oxygen isotope record from high-altitude Lake Petit (2200 m a.s.l.) in the Mediterranean Alps: shedding light on a climatic pulse at 4.2 ka. Clim. Past 15, 253–263. https://doi.org/10.5194/cp-15-253-2019.
Chao, A., Gotelli, N.J., Hsieh, T.C., Sander, E.L., Ma, K.H., Colwell, R.K., Ellison, A.M., 2014. Rarefaction and extrapolation with Hill numbers: a framework for sampling and estimation in species diversity studies. Ecol. Monogr. 84, 45–67. https://doi.org/10.1890/13-0133.1.
Chapligin, B., Leng, M.J., Webb, E., Alexandre, A., Dodd, J.P., Ijiri, A., Lücke, A., Shemesh, A., Abelmann, A., Herzschuh, H., Longstaffe, F.J., Meyer, H., Moschen, R., Okazaki, Y., Rees, N.H., Sharp, Z.D., Sloane, H.J., Sonzongi, C., Swann, J.E.A., Sylvestre, F., Tyler, J.J., Yam, R., 2011. Inter-laboratory comparison of oxygen isotope compositions from biogenic silica. Geochem. Cosmochim. Acta 75, 7242–7256. https://doi.org/10.1016/j.gca.2011.08.011.
Chapligin, B., Meyer, H., Bryan, A., Snyder, J., Kemnitz, H., 2012a. Assessment of purification and contamination correction methods for analysing the oxygen isotope composition from biogenic silica. Chem. Geol. 300–301, 185–199. https://doi.org/10.1016/j.chemgeo.2012.01.004.
Chapligin, B., Meyer, H., Friedrichsen, H., Marent, A., Sohns, E., Hubberten, H.-W., 2010. A high-performance, safer and semi-automated approach for the $\delta^{18}O$ analysis of diatom silica and new methods for removing exchangeable oxygen. Rapid Commun. Mass Spectrom. 24, 2655–2664. https://doi.org/10.1002/rcm.4689.
Chapligin, B., Meyer, H., Swann, G.E.A., Meyer-Jacob, C., Hubberten, H.-W., 2012b. A 250 ka oxygen isotope record from diatoms at Lake El'gygytgyn, far east Russian Arctic. Clim. Past 8, 1621–1636. https://doi.org/10.5194/cp-8-1621-2012.
Cherdonova (Atlasova), V.S., 1993. Types of circulation processes and its frequency in southern Yakutia. Questions Geogr. Yakutia 7, 17–25 (in Russian).
Clayton, R., Mayeda, T., 1963. The use of bromine pentafluoride in the extraction of oxygen from oxides and silicates for isotopic analysis. Geochem. Cosmochim. Acta 27, 43–52. https://doi.org/10.1016/0016-7037(63)90071-1.
Craig, H., 1961. Isotopic variations in meteoric waters. Science 133, 1702–1703. https://doi.org/10.1126/science.133.3465.1702.
Dansgaard, W., 1964. Stable isotopes in precipitation. Tellus 16 (4), 436–468. https://doi.org/10.1111/j.2153-3490.1964.tb00181.x.
Davydova, N.N., 1985. Diatoms – Indicators of the Environmental Conditions of Water-Bodies in the Holocene. Publishing House Nauka, Leningrad (in Russian).
Desyatkin, R., Fedorov, A., Desyatkin, A., Konstantinov, P., 2015. Air temperature changes and their impact on permafrost ecosystems in Eastern Siberia. Therm. Sci. 19 (2), S351–S360. https://doi.org/10.2298/TSCI150320102D.
Diekmann, B., Pestryakova, L., Nazarova, L., Subetto, D., Tarasov, P.E., Stauch, G., Thiemann, A., Lehmkuhl, F., Biskaborn, B.K., Kuhn, G., Henning, D., Müller, S., 2016. Late Quaternary lake dynamics in the Verkhoyansk mountains of eastern Siberia: implications for climate and glaciation history. Polarforschung 86 (2), 97–110. https://doi.org/10.2312/polarforschung.86.2.97.
Dodd, J.P., Sharp, Z.D., 2010. A laser fluorination method for oxygen isotope analysis of biogenic silica and a new oxygen isotope calibration of modern diatoms in freshwater environments. Geochem. Cosmochim. Acta 74, 1381–1390. https://doi.org/10.1016/j.gca.2009.11.023.
Draxler, R.R., Hess, G.D., 1998. An overview of the HYSPLIT_4 modelling system for trajectories, dispersion and deposition. Aust. Meteorol. Mag. 47, 295–308.
Draxler, R.R., Rolph, G.D., 2015. HYSPLIT (HYbrid Single-Particle Lagrangian Integrated Trajectory) Model Access via NOAA ARL READY Website. Silver Spring. NOAA Air Resources Laboratory, MD. https://ready.arl.noaa.gov/HYSPLIT.php.
Duff, K.E., Laing, T.E., Smol, J.P., Lean, D.R.S., 1999. Limnological characteristics of lakes located across arctic treeline in northern Russia. Hydrobiologia 391, 205–222. https://doi.org/10.1023/A:1003542322519.
Fedorov, A.N., Gavriliev, P.P., Konstantinov, P.Y., Hiyama, T., Iijima, Y., Iwahana, G., 2014. Estimating the water balance of a thermokarst lake in the middle of the Lena River basin, eastern Siberia. Ecohydrology 7, 188–196. https://doi.org/10.1002/eco.1378.
Filatova, N.I., Khain, V.E., 2008. Development of the Verkhoyansk-Kolyma orogenic system as a result of interaction of adjacent continental and oceanic plates. Geotectonics 42 (4), 258–285. https://doi.org/10.1134/S001685210804002X.
Fradkina, A.F., Alekseev, M.N., Andreev, A.A., Klimanov, V.A., 2005. East Siberia (based on data obtained mainly in Central Yakutia). In: Velichko, A.A., Nechaev, V.P. (Eds.), Cenozoic Climatic and Environmental Changes in Russia, vol. 382. Geol. Soc. Am. Spec. Pap, pp. 89–103.
Frost, G.V., Epstein, H.E., 2014. Tall shrub and tree expansion in Siberian tundra ecotones since the 1960s. Global Change Biol. 20, 1264–1277. https://doi.org/10.1111/gcb.12406.
Gavrilova, M.K., 1973. Climate of Central Yakutia. Yakutbook Publishing House, Yakutsk (in Russian).
Gleser, S.I., Jouse, A.P., Marakova, I.V., Proschkina-Lavrenko, A.I., Sheshukova-Poretzkaja, V.S. (Eds.), 1974. The Diatoms of the USSR (Fossil and Recent), vol. 1. Publishing House Nauka, Leningrad Branch, Leningrad (in Russian).
Gleser, S.I., Marakova, I.V., Moisseeva, A.I., Nikolaev, V.A. (Eds.), 1988. The Diatoms of the USSR (Fossil and Recent), vols. II-1. Publishing House Nauka, Leningrad Branch, Leningrad (in Russian).
Gleser, S.I., Marakova, I.V., Moisseeva, A.I., Nikolaev, V.A. (Eds.), 1992. The Diatoms of the USSR (Fossil and Recent), vols. II-1. Publishing House Nauka, Leningrad Branch, Leningrad (in Russian).
Glushkov, A.V., 2016. Rivers of Eastern Russia. Yakutsk. (in Russian).
Grimm, E.C., 1987. CONISS: a FORTRAN 77 program for stratigraphically constrained cluster analysis by the method of incremental sum of squares. Comput. Geosci. 13 (1), 13–35. https://doi.org/10.1016/0098-3004(87)90022-7.
Harding, P., Bezrukova, E.V., Kostrova, S.S., Lacey, J.H., Leng, M.J., Meyer, H., Pavlova, L.A., Shchetnikov, A., Shtenberg, M.V., Tarasov, P.E., Mackay, A.W., 2020. Hydrological (in)stability in southern Siberia during the Younger Dryas and early Holocene. Global Planet. Change 195, 103333. https://doi.org/10.1016/j.gloplacha.2020.103333.
Haworth, E.Y., 1975. A scanning electron microscope study of some different frustule forms of the genus *Fragilaria* found in Scottish late-glacial sediments. Br. Phycol. J. 10, 73–80. https://doi.org/10.1080/00071617500650071.
Haworth, E.Y., 1976. Two late-glacial (late Devensian) diatom assemblage profiles from northern Scotland. New Phytol. 77, 227–256. https://doi.org/10.1111/j.1469-8137.1976.tb01516.x.
Herzschuh, U., Pestryakova, L.A., Savelieva, L.A., Heinecke, L., Böhmer, Th., Biskaborn, B.K., Andreev, A., Ramisch, A., Shinneman, A.L.C., Birks, H.J.B., 2013. Siberian larch forests and the ion content of thaw lakes form a geochemically functional entity. Nat. Commun. 4, 2408. https://doi.org/10.1038/ncomms3408.
Hill, M.O., 1973. Diversity and evenness: a unifying notation and its consequences. Ecology 54 (2), 427–432. https://doi.org/10.2307/1934352.
IAEA/WMO, 2020. Global Network of isotopes in precipitation. The GNIP database. https://nucleus.iaea.org/wiser.
IPCC, 2014. In: Core Writing Team, Pachauri, R.K., Meyer, L.A. (Eds.), Climate Change 2014: Synthesis Report. Contribution of Working Groups I, II and III to the Fifth Assessment Report of the Intergovernmental Panel on Climate Change. IPCC, Geneva, Switzerland.
Jorgenson, M., Shur, Y., Pullman, E., 2006. Abrupt increase in permafrost degradation in Arctic Alaska. Geophys. Res. Lett. 33, L02503. https://doi.org/10.1029/2005GL024960.
Juillet-Leclerc, A., Labeyrie, L., 1987. Temperature dependence of the oxygen isotopic fractionation between diatom silica and water. Earth Planet Sci. Lett. 84, 69–74. https://doi.org/10.1016/0012-821X(87)90177-4.
Kaufman, D., McKay, N., Routson, C., Erb, M., Davis, B., Heiri, O., Jaccard, S., Tierney, J., Dätwyler, C., Axford, Y., Brussel, T., Cartapanis, O., Chase, B., Dawson, A., de Vernal, A., Engels, S., Jonkers, L., Marsicek, J., Moffa-Sánchez, P., Morrill, C., Orsi, A., Rehfeld, K., Saunders, K., Sommer, P.S., Thomas, E., Tonello, M., Tóth, M., Vachula, R., Andreev, A., Bertrand, S., Biskaborn, B., Bringué, M., Brooks, S., Caniupán, M., Chevalier, M., Cwynar, L., Emile-Geay, J., Fegyveresi, J., Feurdean, A., Finsinger, W., Fortin, M.-C., Foster, L., Fox, M., Gajewski, K., Grosjean, M., Hausmann, S., Heinrichs, M., Holmes, N., Ilyashuk, B., Ilyashuk, E., Juggins, S., Khider, D., Koinig, K., Langdon, P., Larocque-Tobler, I., Li, J., Lotter, A., Luoto, T., Mackay, A., Magyari, E., Malevich, S., Mark, B., Massaferro, J., Montade, V., Nazarova, L., Novenko, E., Parducci, L., Pearson, E., Peros, M., Pienitz, R., Płóciennik, M., Porinchu, D., Potito, A., Rees, A., Reinemann, S., Roberts, S., Rolland, N., Salonen, S., Self, A., Seppä, H., Shala, S., St-Jacques, J.-M., Stenni, B., Syrykh, L., Tarrats, P., Taylor, K., van den Bos, V., Velle, G., Wahl, E., Walker, I., Wilmshurst, J., Zhang, E., Zhilich, S., 2020. A global database of Holocene paleotemperature records. Sci. Data 7, 115. https://doi.org/10.1038/s41597-020-0445-3.
Kaufman, D.S., Ager, T.A., Anderson, N.J., Anderson, P.M., Andrews, J.T., Bartlein, P.J., Brubaker, L.B., Coats, L.L., Cwynar, L.C., Duvall, M.L., Dyke, A.S., Edwards, M.E., Eisner, W.R., Gajewski, K., Geirsdóttir, A., Hu, F.S., Jennings, A.E., Kaplan, M.R., Kerwin, M.W., Lozhkin, A.V., MacDonald, G.M., Miller, G.H., Mock, C.J., Oswald, W.W., Otto-Bliesner, B.L., Porinchu, D.F., Rühland, K., Smol, J.P., Steig, E.J., Wolfe, B.B., 2004. Holocene thermal maximum in the western Arctic (0–180°W). Quat. Sci. Rev. 23, 529–560. https://doi.org/10.1016/j.quascirev.2003.09.007.
Khaliullina, L. Yu., Frolova, L.A., Volkova, T.S., Pestryakova, L.A., 2016. Species composition of planktonic algae of termokarst lakes of Khatanga River basin (Krasnoyarsk Region, Russia). Res. J. Pharmaceut. Biol. Chem. Sci. 7 (5), 1329–1340.
Kleinen, T., Tarasov, P., Brovkin, V., Andreev, A., Stebich, M., 2011. Comparison of modeled and reconstructed changes in forest cover through the past 8000 years: Eurasian perspective. Holocene 21, 723–734. https://doi.org/10.1177/0959683610386980.
Klemm, J., Herzschuh, U., Pestryakova, L.A., 2016. Vegetation, climate and lake changes over the last 7000 years at the boreal treeline in north-central Siberia. Quat. Sci. Rev. 147, 422–434. https://doi.org/10.1016/j.quascirev.2015.08.015.
Klemm, J., Herzschuh, U., Pisaric, M.F.J., Telford, R.J., Heim, B., Pestryakova, L.A., 2013. A pollen-climate transfer function from the tundra and taiga vegetation in Arctic Siberia and its applicability to a Holocene record. Palaeogeogr. Palaeoclimatol. Palaeoecol. 386, 702–713. https://doi.org/10.1016/j.palaeo.2013.06.033.
Kobe, F., Bezrukova, E.V., Leipe, C., Shchetnikov, A.A., Goslar, T., Wagner, M., Kostrova, S.S., Tarasov, P.E., 2020. Holocene vegetation and climate history in Baikal Siberia reconstructed from pollen records and its implications for archaeology. Archaeol. Res. Asia 23, 100209. https://doi.org/10.1016/j.ara.2020.100209.
Komarenko, L.E., Vasilyeva, I.I., 1975. Freshwater Diatoms and Blue-Green Algae of Yakutian Waters. Publishing House Nauka, Moscow (in Russian).
Kostrova, S.S., Meyer, H., Bailey, H.L., Ludikova, A.V., Gromig, R., Kuhn, G., Shibaev, Y.A., Kozachek, A.V., Ekaykin, A.A., Chapligin, B., 2019. Holocene

hydrological variability of Lake Ladoga, northwest Russia, as inferred from diatom oxygen isotopes. Boreas 48, 361–376. https://doi.org/10.1111/bor.12385.
Kostrova, S.S., Meyer, H., Chapligin, B., Kossler, A., Bezrukova, E.V., Tarasov, P.E., 2013. Holocene oxygen isotope record of diatoms from Lake Kotokel (southern Siberia, Russia) and its palaeoclimatic implications. Quat. Int. 290–291, 21–34. https://doi.org/10.1016/j.quaint.2012.05.011.
Kostrova, S.S., Meyer, H., Chapligin, B., Tarasov, P.E., Bezrukova, E.V., 2014. The last glacial maximum and late glacial environmental and climate dynamics in the Baikal region inferred from an oxygen isotope record of lacustrine diatom silica. Quat. Int. 348, 25–36. https://doi.org/10.1016/j.quaint.2014.07.034.
Kostrova, S.S., Meyer, H., Fernandoy, F., Werner, M., Tarasov, P.E., 2020. Moisture origin and stable isotope characteristics of precipitation in southeast Siberia. Hydrol. Process. 34, 51–67. https://doi.org/10.1002/hyp.13571.
Krammer, K., 2000. The genus Pinnularia. In: Lange-Bertalot, H. (Ed.), Diatoms of Europe: Diatoms of the European Inland Waters and Comparable Habitats. A.R.G. Gantner Verlag K.G., Ruggell.
Krammer, K., 2002. Cymbella. In: Lange-Bertalot, H. (Ed.), Diatoms of Europe: Diatoms of the European Inland Waters and Comparable Habitats. A.R.G. Gantner Verlag K.G., Ruggell.
Krammer, K., 2003. Cymbopleura, Delicata, Navicymbula, Gomphocymbellopsis, Afrocymbella. In: Lange-Bertalot, H. (Ed.), Diatoms of Europe: Diatoms of the European Inland Waters and Comparable Habitats. A.R.G. Gantner Verlag K.G., Ruggell.
Krammer, K., Lange-Bertalot, H., 1991. Bacillariophyceae. In: Ettl, H., Gerloff, J., Heying, H., Mollenhauer, D. (Eds.), Süßwasserflora von Mitteleuropa. Band 2/3. Gustav Fischer Verlag, Jena.
Krammer, K., Lange-Bertalot, H., 1999a. Bacillariophyceae 1. Teil: Naviculaceae. In: Ettl, G.J., Gerloff, H., Heynig, J., Mollenhauer, H. (Eds.), Süßwasserflora von Mitteleuropa. Band 2/1. Gustav Fischer Verlag, Heidelberg.
Krammer, K., Lange-Bertalot, H., 1999b. Bacillariophyceae 2. Teil: Bacillariaceae, Epithemiaceae, Surirellaceae. In: Ettl, H., Gerloff, J., Heynig, H., Mollenhauer, D. (Eds.), Süßwasserflora von Mitteleuropa. Band 2/2. Gustav Fischer Verlag, Heidelberg.
Krammer, K., Lange-Bertalot, H., 2000. Bacillariophyceae 3. Teil: Centrales, Fragilariaceae, Eunotiaceae. In: Ettl, H., Gerloff, J., Heynig, H., Mollenhauer, D. (Eds.), Süßwasserflora von Mitteleuropa. Band 2/3. Gustav Fischer Verlag, Heidelberg.
Krklec, K., Domínguez-Villar, D., 2014. Quantification of the impact of moisture source regions on the oxygen isotope composition of precipitation over Eagle Cave, central Spain. Geochem. Cosmochim. Acta 134, 39–54. https://doi.org/10.1016/j.gca.2014.03.011.
Kumke, Th., Ksenofontova, M., Pestryakova, L., Nazarova, L., Hubberten, H.-W., 2007. Limnological characteristics of lake in the lowlands of Central Yakutia, Russia. J. Limnol. 66 (1), 40–53. https://doi.org/10.4081/jlimnol.2007.40.
Kurita, N., 2011. Origin of Arctic water vapor during the ice-growth season. Geophys. Res. Lett. 38, L02709. https://doi.org/10.1029/2010GL046064.
Labeyrie, L.D., 1974. New approach to surface seawater palaeotemperatures using $^{18}O/^{16}O$ ratios in silica of diatom frustules. Nature 248, 40–42. https://doi.org/10.1038/248040a0.
Lange-Bertalot, H., 2001. Navicula sensu stricto.10 genera separated from Navicula sensu lato Frustulia. In: Lange-Bertalot, H. (Ed.), Diatoms of Europe: Diatoms of the European Inland Waters and Comparable Habitats. A.R.G. Gantner Verlag K.G., Ruggell.
Leng, M.J., Barker, P.A., 2006. A review of the oxygen isotope composition of lacustrine diatom silica for palaeoclimate reconstruction. Earth Sci. Rev. 75, 5–27. https://doi.org/10.1016/j.earscirev.2005.10.001.
Letterly, A., Key, J., Liu, Y., 2018. Arctic climate: changes in sea ice extent outweigh changes in snow cover. Cryosphere 12, 3373–3382. https://doi.org/10.5194/tc-12-3373-2018.
Loseva, E.I., 2000. Atlas of Freshwater Pleistocene Diatoms from Northeastern Europe. Publishing House Nauka, St. Petersburg (in Russian).
Mackay, A.W., Swann, G.E.A., Fagel, N., Fietz, S., Morley, D., Rioual, P., Tarasov, P., Leng, M.J., 2013. Hydrological instability during the last Interglacial in Central Asia: a new diatom oxygen isotope record from Lake Baikal. Quat. Sci. Rev. 66, 45–54. https://doi.org/10.1016/j.quascirev.2012.09.025.
Makarova, I.V., Strelnikova, N.I., Kosyrenko, T.F. (Eds.), 2002. The Diatoms of Russia and Adjacent Countries: Fossil and Recent, vols. II-3. Publishing House of St. Petersburg University, St. Petersburg (in Russian).
Mangerud, J., Jakobsson, M., Alexanderson, H., Astakhov, V., Clarke, G.K.C., Henriksen, M., Hjort, C., Krinner, G., Lunkka, J.-P., Möller, P., Murray, A., Nikolskaya, O., Saarnisto, M., Svendsen, J.I., 2004. Ice-dammed lakes and rerouting of the drainage of northern Eurasia during the Last Glaciation. Quat. Sci. Rev. 23, 1313–1332. https://doi.org/10.1016/j.quascirev.2003.12.009.
Marcott, S.A., Shakun, J.D., Clark, P.U., Mix, A.C., 2013. A reconstruction of regional and global temperature for the past 11,300 years. Science 339 (6124), 1198–1201. https://doi.org/10.1126/science.1228026.
Mayewski, P.A., Rohling, E.E., Stager, J.C., Karle, W., Maasch, K.A., Meeker, L.D., Meyerson, E.A., Gasse, F., van Kreveld, Sh, Holmgren, K., Lee-Thorp, J., Rosqvist, G., Rack, F., Staubwasser, M., Schneider, R.R., Steig, E.J., 2004. Holocene climate variability. Quat. Res. 62, 243–255. https://doi.org/10.1016/j.yqres.2004.07.001.
Melles, M., Svendsen, J.I., Fedorov, G., Wagner, B., 2019. Northern Eurasian lakes – late Quaternary glaciation and climate history – introduction. Boreas 48, 269–272. https://doi.org/10.1111/bor.12395.
Merlivat, L., Jouzel, J., 1979. Global climatic interpretation of the deuterium – oxygen 18 relationship for precipitation. J. Geophys. Res. 84 (C8), 5029–5033. https://doi.org/10.1029/JC084iC08p05029.
Meyer, H., Chapligin, B., Hoff, U., Nazarova, L., Diekmann, B., 2015a. Oxygen isotope composition of diatoms as late Holocene climate proxy at two-Yurts lake, central Kamchatka, Russia. Global Planet. Change 134, 118–128. https://doi.org/10.1016/j.gloplacha.2014.04.008.
Meyer, H., Opel, T., Laepple, T., Dereviagin, A.Yu., Hoffmann, K., Werner, M., 2015b. Long-term winter warming trend in the Siberian Arctic during the mid- to late Holocene. Nat. Geosci. 8, 122–125. https://doi.org/10.1038/ngeo2349.
Meyer, H., Schönicke, L., Wand, U., Hubberten, H.-W., Friedrichsen, H., 2000. Isotope studies of hydrogen and oxygen in ground ice – experiences with the equilibration technique. Isot. Environ. Health Stud. 36, 133–149. https://doi.org/10.1080/10256010008032939.
Miller, G.H., Brigham-Grette, J., Alley, R.B., Anderson, L., Bauch, H.A., Douglas, M.S.V., Edwards, M.E., Elias, S.A., Finney, B.P., Fitzpatrick, J.J., Funder, S.V., Herbert, T.D., Hinzman, L.D., Kaufman, D.S., MacDonald, G.M., Polyak, L., Robock, A., Serreze, M.C., Smol, J.P., Spielhagen, R., White, J.W.C., Wolfe, A.P., Wolff, E.W., 2010. Temperature and precipitation history of the Arctic. Quat. Sci. Rev. 29, 1679–1715. https://doi.org/10.1016/j.quascirev.2010.03.001.
Morgenstern, A., Overduin, P.P., Günther, F., Stettner, S., Ramage, J., Schirrmeister, L., Grigoriev, M.N., Grosse, G., 2021. Thermo-erosional valleys in Siberian ice-rich permafrost. Permafr. Periglac. Process. 32, 59–75. https://doi.org/10.1002/ppp.2087.
Morgenstern, A., Ulrich, M., Günther, F., Roessler, S., Fedorova, I.V., Rudaya, N.A., Wetterich, S., Boike, J., Schirrmeister, L., 2013. Evolution of thermokarst in East Siberian ice-rich permafrost: a case study. Geomorphology 201, 363–379. https://doi.org/10.1016/j.geomorph.2013.07.011.
Müller, S., Tarasov, P.E., Andreev, A.A., Diekmann, B., 2009. Late glacial to Holocene environments in the present-day coldest region of the northern Hemisphere inferred from a pollen record of lake Billyakh, Verkhoyansk Mts, NE Siberia. Clim. Past 5, 73–84. https://doi.org/10.5194/cp-5-73-2009.
Müller, S., Tarasov, P.E., Andreev, A.A., Tütken, T., Gartz, S., Diekmann, B., 2010. Late Quaternary vegetation and environments in the Verkhoyansk Mountains region (NE Asia) reconstructed from a 50-kyr fossil pollen record from Lake Billyakh. Quat. Sci. Rev. 29, 2071–2086. https://doi.org/10.1016/j.quascirev.2010.04.024.
Narancic, B., Pienitz, R., Chapligin, B., Meyer, H., Francus, P., Guilbault, J.-P., 2016. Postglacial environmental succession of Nettilling Lake (Baffin Island, Canadian Arctic) inferred from biogeochemical and microfossil proxies. Quat. Sci. Rev. 147, 391–405. https://doi.org/10.1016/j.quascirev.2015.12.022.
Nazarova, L., Herzschuh, U., Wetterich, S., Kumke, T., Pestryakova, L., 2011. Chironomid-based inference models for estimating mean July air temperature and water depth from lakes in Yakutia, northeastern Russia. J. Paleolimnol. 45, 57–71. https://doi.org/10.1007/s10933-010-9479-4.
Nazarova, L., Lüpfert, H., Subetto, D., Pestryakova, L., Diekmann, B., 2013. Holocene climate conditions in central Yakutia (Eastern Siberia) inferred from sediment composition and fossil chironomids of Lake Temje. Quat. Int. 290–291, 264–274. https://doi.org/10.1016/j.quaint.2012.11.006.
Oksanen, J., Blanchet, F.G., Friendly, M., Kindt, R., Legendre, P., McGlinn, D., Minchin, P.R., O'Hara, R., Simpson, G., Solymos, P., Stevens, M.H.H., Szoecs, E., Wagner, H., 2020. Vegan: community ecology package. R package version 2.5-7. https://github.com/vegandevs/vegan.
Opel, T., Murton, J.B., Wetterich, S., Meyer, H., Ashastina, K., Günther, F., Grotheer, H., Mollenhauer, G., Danilov, P.P., Boeskorov, V., Savvinov, G.N., Schirrmeister, L., 2019. Past climate and continentality inferred from ice wedges at Batagay megaslump in the Northern Hemisphere's most continental region, Yana Highlands, interior Yakutia. Clim. Past 15, 1443–1461. https://doi.org/10.5194/cp-15-1443-2019.
Opel, T., Ulrich, M., 2015. Permafrostdegradation in Sibirien – Sozio-ökonomische Aspekte. In: Lozán, J.L., Grassl, H., Kasang, D., Notz, D., Escher-Vetter, Hrsg, H. (Eds.), Warnsignal Klima: Das Eis der Erde, pp. 261–270 (in German).
Overland, J.E., Hanna, E., Hanssen-Bauer, I., Kim, S.-J., Walsh, J.E., Wang, M., Bhatt, U.S., Thoman, R.L., 2018. Surface air temperature. Arctic report card: update for 2018. https://arctic.noaa.gov/Report-Card/Report-Card-2018.
Oxman, V.S., 2003. Tectonic evolution of the Mesozoic Verkhoyansk–Kolyma belt (NE Asia). Tectonophysics 365, 45–76. https://doi.org/10.1016/S0040-1951(03)00064-7.
Papina, T.S., Malygina, N.S., Eirikh, A.N., Galanin, A.A., Zheleznyak, M.N., 2017. Isotopic composition and sources of atmospheric precipitation in Central Yakutia. Earths Cryosphere 21 (2), 52–61. https://doi.org/10.21782/EC2541-9994-2017-1(52-61.
Pestryakova, L.A., Herzschuh, U., Gorodnichev, R., Wetterich, S., 2018. The sensitivity of diatom taxa from Yakutian lakes (north-eastern Siberia) to electrical conductivity and other environmental variables. Polar Res. 37 (1), 1485625. https://doi.org/10.1080/17518369.2018.1485625.
Pestryakova, L.A., Herzschuh, U., Wetterich, S., Ulrich, M., 2012. Present-day variability and Holocene dynamics of permafrost-affected lakes in central Yakutia (eastern Siberia) inferred from diatom records. Quat. Sci. Rev. 51, 56–70. https://doi.org/10.1016/j.quascirev.2012.06.020.
Popp, S., Belolyubsky, I., Lehmkuhl, F., Prokopiev, A., Siegert, C., Spektor, V., Stauch, G., Diekmann, B., 2007. Sediment provenance of late Quaternary morainic, fluvial and loess-like deposits in the southwestern Verkhoyansk Mountains (eastern Siberia) and implications for regional palaeoenvironmental reconstructions. Geol. J. 42, 477–497. https://doi.org/10.1002/gj.1088.
Popp, S., Diekmann, B., Meyer, H., Siegert, C., Syromyatnikov, I., Hubberten, H.-W., 2006. Palaeoclimate signals as inferred from stable-isotope composition of ground ice in the Verkhoyansk foreland, Central Yakutia. Permafr. Periglac.

Process. 17, 119–132. https://doi.org/10.1002/ppp.556.
R Core Team, 2012. R: A Language and Environment for Statistical Computing. R Foundation for Statistical Computing, Vienna, Austria. https://www.r-project.org.
R Core Team, 2017. R: A Language and Environment for Statistical Computing. R Foundation for Statistical Computing, Vienna, Austria. https://www.r-project.org.
Reimer, P.J., Bard, E., Bayliss, A., Beck, J.W., Blackwell, P.G., Ramsey, C.B., Buck, C.E., Cheng, H., Edwards, R.L., Friedrich, M., Grootes, P.M., Guilderson, T.P., Haflidason, H., Hajdas, I., Hatté, C., Heaton, T.J., Hoffmann, D.L., Hogg, A.G., Hughen, K.A., Kaiser, K.F., Kromer, B., Manning, S.W., Niu, M., Reimer, R.W., Richards, D.A., Scott, E.M., Southon, J.R., Staff, R.A., Turney, C.S.M., van der Plicht, J., 2013. IntCal13 and Marine13 radiocarbon age calibration curves 0–50,000 Years cal BP. Radiocarbon 55, 1869–1887. https://doi.org/10.2458/azu_js_rc.55.16947.
Roland, T.P., Daley, T.J., Caseldine, C.J., Charman, D.J., Turney, C.S.M., Amesbury, M.J., Thompson, G.J., Woodley, E.J., 2015. The 5.2 ka climate event: evidence from stable isotope and multi-proxy palaeoecological peatland records in Ireland. Quat. Sci. Rev. 124, 209–223. https://doi.org/10.1016/j.quascirev.2015.07.026.
Round, F.E., Crawford, R.M., Mann, D.G., 1990. The Diatoms: Biology and Morphology of the Genera. Cambridge University Press, Cambridge.
Rozanski, K., Araguás-Araguás, L., Gonfiantini, R., 1993. Isotopic patterns in modern global precipitation. In: Climate Change in Continental Isotope Records. Geophysical Monograph, vol. 78. American Geophysical Union Monograph, pp. 1–36.
Rudaya, N., Tarasov, P., Dorofeyuk, N., Solovieva, N., Kalugin, I., Andreev, A., Daryin, A., Diekmann, B., Riedel, F., Tserendash, N., Wagner, M., 2009. Holocene environments and climate in the Mongolian Altai reconstructed from the Hoton-Nur pollen and diatom records: a step towards better understanding climate dynamics in Central Asia. Quat. Sci. Rev. 28, 540–554. https://doi.org/10.1016/j.quascirev.2008.10.013.
Rudenko, O., Taldenkova, E., Ovsepyan, Ya., Stepanova, A., Bauch, H.A., 2020. A multiproxy-based reconstruction of the mid- to late Holocene paleoenvironment in the Laptev sea off the Lena river Delta (Siberian arctic). Palaeogeogr. Palaeoclimatol. Palaeoecol. 540, 109502. https://doi.org/10.1016/j.palaeo.2019.109502.
Rühland, K.M., Paterson, A.M., Smol, J.P., 2015. Lake diatom responses to warming: reviewing the evidence. J. Paleolimnol. 54, 1–35. https://doi.org/10.1007/s10933-015-9837-3.
Safronov, V.M., 2016. Climate change and Mammals of Yakutia. Biol. Bull. Russ. Acad. Sci. 43 (9), 1256–1270. https://doi.org/10.1134/S1062359016110121.
Saros, J.E., Anderson, N.J., 2015. The ecology of the planktonic diatom *Cyclotella* and its implications for global environmental change studies. Biol. Rev. 90, 522–541. https://doi.org/10.1111/brv.12120.
Schleusner, P., Biskaborn, B.K., Kienast, F., Wolter, J., Subetto, D., Diekmann, B., 2015. Basin evolution and palaeoenvironmental variability of the thermokarst lake El'gene-Kyuele, Arctic Siberia. Boreas 44, 216–229. https://doi.org/10.1111/bor.12084.
Shahgedanova, M., Perov, V., Mudrov, Y., 2002. The mountains of Northern Russia. In: Shahgedanova, M. (Ed.), The Physical Geography of Northern Eurasia. Oxford University Press, Oxford, pp. 284–313.
Shestakova, A.A., Toropov, P.A., Matveeva, T.A., 2020. Climatology of extreme downslope windstorms in the Russian Arctic. Weather. Clim. Extremes 28, 100256. https://doi.org/10.1016/j.wace.2020.100256.
Shiklomanov, A., Lammers, R., 2014. River ice responses to a warming Arctic – recent evidence from Russian rivers. Environ. Res. Lett. 9, 035008 https://doi.org/10.1088/1748-9326/9/3/035008.
Smith, L.C., Sheng, Y., MacDonald, G.M., Hinzman, L.D., 2005. Disappearing arctic lakes. Science 308, 1429. https://doi.org/10.1126/science.1108142.
Snape, T.J., Forster, P.M., 2014. Decline of Arctic sea ice: evaluation and weighting of CMIP5 projections. Geophys. Res. Atmos. 119 (2), 546–554. https://doi.org/10.1002/2013JD020593.
Stauch, G., Lehmkuhl, F., 2010. Quaternary glaciations in the Verkhoyansk mountains, northeast Siberia. Quat. Res. 74, 145–155. https://doi.org/10.1016/j.yqres.2010.04.003.
Stein, A.F., Draxler, R.R., Rolph, G.D., Stunder, B.J.B., Cohen, M.D., Ngan, F., 2015. NOAA's HYSPLIT atmospheric transport and dispersion modeling system. Bull. Am. Meteorol. Soc. 96, 2059–2077. https://doi.org/10.1175/BAMS-D-14-00110.1.
Streletskiy, D., Anisimov, O., Vasiliev, A., 2015a. Permafrost degradation. In: Haeberli, W., Whiteman, C., Shroder, J.F. (Eds.), Snow and Ice-Related Hazards, Risks, and Disasters. Academic Press, pp. 303–344.
Streletskiy, D.A., Tananaev, N.I., Opel, Th., Shiklomanov, N.I., Nyland, K.E., Streletskaya, I.D., Tokarev, I., Shiklomanov, A.I., 2015b. Permafrost hydrology in changing climatic conditions: seasonal variability of stable isotope composition in rivers in discontinuous permafrost. Environ. Res. Lett. 10, 095003 https://doi.org/10.1088/1748-9326/ab282f.
Sutton, J.N., André, L., Cardinal, D., Conley, D.J., de Souza, G.F., Dean, J., Dodd, J., Ehlert, C., Ellwood, M.J., Frings, P.J., Grasse, P., Hendry, K., Leng, M.J., Michalopoulos, P., Panizzo, V.N., Swann, G.E.A., 2018. A review of the stable isotope bio-geochemistry of the global silicon cycle and its associated trace elements. Front. Earth Sci. 5, 112. https://doi.org/10.3389/feart.2017.00112.
Svendsen, J.I., Færseth, L.M.B., Gyllencreutz, R., Haflidason, H., Henriksen, M., Hovland, M.N., Lohne, Ø.S., Mangerud, J., Nazarov, D., Regnéll, C., Schaefer, J.M., 2019. Glacial and environmental changes over the last 60 000 years in the Polar Ural Mountains, Arctic Russia, inferred from a high-resolution lake record and other observations from adjacent areas. Boreas 48, 407–431. https://doi.org/10.1111/bor.12356.
Svensson, A., Andersen, K.K., Bigler, M., Clausen, H.B., Dahl-Jensen, D., Davies, S.M., Johnsen, S.J., Muscheler, R., Parrenin, F., Rasmussen, S.O., Röthlisberger, R., Seierstad, I., Steffensen, J.P., Vinther, B.M., 2008. A 60 000 year Greenland stratigraphic ice core chronology. Clim. Past 4, 47–57. https://doi.org/10.5194/cp-4-47-2008.
Swann, G.E.A., Leng, M.J., 2009. A review of diatom $\delta^{18}O$ in palaeoceanography. Quat. Sci. Rev. 28, 384–398. https://doi.org/10.1016/j.quascirev.2008.11.002.
Swann, G.E.A., Leng, M.J., Juschus, O., Melles, M., Brigham-Grette, J., Sloane, H.J., 2010. A combined oxygen and silicon diatom isotope record of Late Quaternary change in Lake El'gygytgyn, North East Siberia. Quat. Sci. Rev. 29, 774–786. https://doi.org/10.1016/j.quascirev.2009.11.024.
Swann, G.E.A., Mackay, A.W., Vologina, E., Jones, M.D., Panizzo, V.N., Leng, M.J., Sloane, H.J., Snelling, A.M., Sturm, M., 2018. Lake Baikal isotope records of Holocene central Asian precipitation. Quat. Sci. Rev. 189, 210–222. https://doi.org/10.1016/j.quascirev.2018.04.013.
Tarasov, P.E., Müller, S., Zech, M., Andreeva, D., Diekmann, B., Leipe, C., 2013. Last glacial vegetation reconstructions in the extreme-continental eastern Asia: potentials of pollen and n-alkane biomarker analyses. Quat. Int. 290–291, 253–263. https://doi.org/10.1016/j.quaint.2012.04.007.
Ulrich, M., Matthes, H., Schmidt, J., Fedorov, A.N., Schirrmeister, L., Siegert, C., Schneider, B., Strauss, J., Zielhofer, C., 2019. Holocene thermokarst dynamics in Central Yakutia – a multi-core and robust grain-size endmember modeling approach. Quat. Sci. Rev. 218, 10–33. https://doi.org/10.1016/j.quascirev.2019.06.010.
van Hardenbroek, M., Chakraborty, A., Davies, K.L., Harding, P., Heiri, O., Henderson, A.C.G., Holmes, J.A., Lasher, G.E., Leng, M.J., Panizzo, V.N., Roberts, L., Schilder, J., Trueman, C.N., Wooller, M.J., 2018. The stable isotope composition of organic and inorganic fossils in lake sediment records: current understanding, challenges, and future directions. Quat. Sci. Rev. 196, 154–176. https://doi.org/10.1016/j.quascirev.2018.08.003.
Vyse, S.A., Herzschuh, U., Andreev, A.A., Pestryakova, L.A., Diekmann, B., Armitage, S.J., Biskaborn, B.K., 2020. Geochemical and sedimentological responses of arctic glacial Lake Ilirney, chukotka (far east Russia) to palaeoenvironmental change since ~51.8 ka BP. Quat. Sci. Rev. 247, 106607. https://doi.org/10.1016/j.quascirev.2020.106607.
Wanner, H., Beer, J., Bütikofer, J., Crowley, T.J., Cubasch, U., Flückiger, J., Goosse, H., Grosjean, M., Joos, F., Kaplan, J.O., Küttel, M., Müller, S.A., Prentice, I.C., Solomina, O., Stocker, T.F., Tarasov, P., Wagner, M., Widmann, M., 2008. Mid- to late Holocene climate change: an overview. Quat. Sci. Rev. 27, 1791–1828. https://doi.org/10.1016/j.quascirev.2008.06.013.
Werner, K., Tarasov, P.E., Andreev, A.A., Müller, S., Kienast, F., Zech, M., Zech, W., Diekmann, B., 2010. A 12.5-kyr history of vegetation dynamics and mire development with evidence of Younger Dryas larch presence in the Verkhoyansk Mountains, East Siberia, Russia. Boreas 39, 56–68. https://doi.org/10.1111/j.1502-3885.2009.00116.x.
Wetterich, S., Herzschuh, U., Meyer, H., Pestryakova, L., Plessen, B., Lopez, C.M.L., Schirrmeister, L., 2008. Evaporation effects as reflected in freshwaters and ostracod calcite from modern environments in Central and Northeast Yakutia (East Siberia, Russia). Hydrobiologia 614, 171–195. https://doi.org/10.1007/s10750-008-9505-y.
Wiese, V.Yu., 1927. The Climate of Yakutia. Publishing House of the Academy of Sciences of the USSR, Leningrad (in Russian).
Zhirkov, I.I., 2000. Classification of lakes of central Yakutia. In: Lakes of Cold Regions. Questions of Theoretic, Methods, Limnogenesis, Classifications and Typologies. Yakutsk State University, Yakutsk, pp. 84–93 (in Russian).